International Journal of Non–Linear Mechanics 161 (2024) 104672

Contents lists available at ScienceDirect

International Journal of Non-Linear Mechanics

journal homepage: www.elsevier.com/locate/nlm

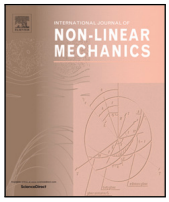

Cytokine-induced instabilities in a reaction–diffusion-chemotaxis model of Multiple Sclerosis: Bifurcation analysis and well-posedness☆

F. Gargano [b], M.C. Lombardo [a], R. Rizzo [b], M. Sammartino [b,*], V. Sciacca [a]

[a] Dept of Mathematics, University of Palermo, Via Archirafi 34, 90123 Palermo, Italy
[b] Dept of Engineering, University of Palermo, viale delle Scienze Ed.8, 90128 Palermo, Italy

ARTICLE INFO

MSC:
92C15
92C17
92C37
92C40

Keywords:
Multiple Sclerosis
Inflammation
Chemotaxis PDE model
Well-posedness
Turing instability
Bifurcation analysis

ABSTRACT

In this paper, we develop a model for the evolution of the Multiple Sclerosis pathology that considers the modulatory influence of cytokines on the activation rate of macrophages. Our starting point is the reaction–diffusion-chemotaxis model proposed in 4, and we modify the macrophage activation mechanism. What triggers the immune cells into an active state is still debated in the medical literature. In this paper, we explore the hypothesis, e.g., Lassmann, (2018), that cytokines mediate the activation mechanism. Our primary focus is on the rigorous analysis of instabilities responsible for the formation of demyelinating lesions and on the qualitative properties of the solution.

Through a weakly nonlinear analysis, we characterize the chemotaxis-driven Turing instability and construct the stationary patterns that emerge from this instability. Using biologically relevant parameter values, we show that the asymptotic solutions of our model system reproduce the concentric demyelinating rings, confluent plaques, and preactive lesions observed in Balò sclerosis and type III Multiple Sclerosis. Furthermore, we explore the initiation and progression of demyelinated plaques through extensive numerical simulations on two-dimensional domains. Our findings reveal that the alternative scenario proposed here results in a less aggressive pathology characterized by reduced inflammation levels and significantly slower disease progression.

Under the appropriate regularity conditions on the initial data, we prove the existence of a unique global solution to our proposed system.

This study provides insights into the role of cytokines in the pathogenesis of Multiple Sclerosis, shedding light on the disease's dynamics and offering potential avenues for therapeutic interventions.

1. Introduction

In this introductory Section, we shall first discuss the primary mechanisms that underlie the etiopathogenesis of various types of Multiple Sclerosis (MS), according to the general consensus. Specifically, we shall focus on the distinct roles played by innate and adaptive immunity in different types of MS. In the second Subsection, we shall provide an overview of the main attempts to give a mathematical description of MS: probably due to the disorder's complexity and heterogeneity, initial contributions were formulated only in recent years, leading to a relatively underdeveloped body of literature on the subject. In the third Subsection, we shall present the main results of this paper. They involve modeling and analyzing the impact of cytokines on the activation of the inflammatory cascade leading to demyelination, and the proof of the well-posedness of the model. In the last Subsection, we shall present the plan of the paper.

1.1. MS pathology: a brief overview

Multiple Sclerosis is one of the most common autoimmune disabling and degenerative disorders of the Central Nervous System (CNS) that affects over 2.8 million people worldwide. MS patients often experience relapsing–remitting phases on a background of a progressive disease course until progression becomes dominant [1–3]. The disease is characterized by a loss of myelin, a fatty substance that is produced by oligodendrocytes and that, surrounding the nerve fibers of CNS, favors the propagation of the electric signal along the nerve axon. Destruction of myelin sheaths is usually organized in pseudo-circular areas, called plaques or lesions [1–3].

An important line of research in MS focuses on understanding the complex mechanisms underlying the pathology, particularly those

☆ In dedication to Giuseppe Saccomandi, with friendship.

* Corresponding author.
E-mail addresses: francesco.gargano@unipa.it (F. Gargano), mariacarmela.lombardo@unipa.it (M.C. Lombardo), rossella.rizzo@unipa.it (R. Rizzo), marco.sammartino@unipa.it (M. Sammartino), vincenzo.sciacca@unipa.it (V. Sciacca).

https://doi.org/10.1016/j.ijnonlinmec.2024.104672
Received 6 December 2023; Received in revised form 6 February 2024; Accepted 9 February 2024
Available online 17 February 2024

related to etiology and its correlation with the observed clinical and immunological heterogeneity, both at the population and individual level. It is generally accepted that a dysfunction of the immune system causes MS, which mistakes healthy neural cells for diseased or damaged ones [1,3–5]. Recent studies indicate that immune cells of both the innate and adaptive immune system are involved in the onset and development of MS [2,3].

Among the cells of the innate immune system, microglia and macrophages play a prominent role in the pathogenesis of MS [2]. Microglia, small-size white blood cells present in the CNS, manage the entire defense system in the brain, as other larger immune cells cannot cross the blood–brain barrier (BBB) under physiologic conditions. Microglia periodically sweep the brain tissue, looking for pathogens, foreign cells, or damaged neurons. In the presence of foreign or damaged cells, they turn into an *active* state, *i.e.* they increase their size and phagocytize harmful cells [6–9]. In the phagocytic state, microglia look like other macrophages (from the Greek *makròs phagein*, *i.e.*, *big eater*), which are immune cells (or white blood cells) specialized to digest pathogens and foreign substances [9,10]. In healthy organisms, macrophages are not present in the CNS; they can be found in the perivascular space and are too large to cross the BBB. However, in MS brains, the BBB has increased permeability, and even large cells such as macrophages are able to cross the barrier and infiltrate the CNS [6–9]. In fact, infiltrating macrophages and microglia are the dominant immune cells in plaques and are thought to be mainly responsible for neuroinflammation and myelin degradation of MS patients [4,6,9,11,12]. On the other hand, macrophages also play many beneficial roles, including removing neurotoxins and promoting repair. According to their functional roles, macrophages are roughly divided into two subtypes: pro-inflammatory (or M1) and anti-inflammatory (or M2) macrophages [5–7,13]. Both M1 and M2 macrophages release cytokines, small proteins that mediate and regulate immune responses, inflammatory reactions, and chemotaxis, and lead to the proliferation of antibody cells [11,14,15].

Because MS lesions exhibit profound heterogeneity with respect to their immunopathologic patterns, several classification systems based on plaque activity and histologic features have been introduced. Based on biopsy and autopsy specimens, a classification of early active lesions known as the Lucchinetti/Lassmann/Brück system (LLB classification) has recently been proposed [16–19], which divides the actively demyelinating lesions into four distinct subtypes. Type I and type II lesions are the most common. They are characterized by high macrophage and lymphocyte infiltration levels, complement activation, and massive phagocytosis of myelin by macrophages. Type-I and type-II plaques closely resemble the lesions seen in T-cell mediated experimental autoimmune encephalomyelitis, a murine model of brain inflammation. Type III lesions resemble hypoxia-like lesions and are characterized by extensive oligodendrocyte apoptosis in regions of myelin preservation, high activation of microglia and macrophages, no signs of complement activation and low levels of lymphocyte infiltration [16,20,21]. Similar immunopathological features are also reported in Baló sclerosis, a rare, aggressive variant of MS whose plaques display concentric alternating rims of demyelinated and myelinated tissue [22]. Finally, type IV lesions are infrequent and, most likely, caused by oligodendrocyte dysfunction. Immunohistological classification suggests that different mechanisms may cause different subtypes of MS lesions. Specifically, type I and type II MS would be autoimmune-mediated disorders, whereas type III lesions emerge from microglia activation through innate immunity mechanisms. Lesions would be the result of an initial oligodendrocyte injury, caused by oxygen and nitrogen radicals released by activated microglia, ultimately followed by T-cells infiltration and demyelination, leading to the formation of the classical plaque [18,19,21]. Whether different lesion types are specific to each MS patient [16] or if they correspond to different temporal stages of the disease [18,20,21], is still under debate in the biomedical community.

1.2. Mathematical modeling of MS

In recent decades, mathematical modeling of diseases has been widely used to study and explore the mechanisms responsible for the development of severe pathologies such as cancer, diabetes, respiratory syndromes, inflammation [23–25] and, only to a lesser extent, autoimmune diseases [26]. With few exceptions, existing continuum deterministic models of MS are formulated in terms of ordinary differential equations (ODEs), in which the species distribution is assumed uniform in space, and one takes into account only its time dependence. Such models can reproduce the oscillatory behavior of immune cells corresponding to the relapsing–remitting phase of MS and, in some cases, also the underlying progressive stage (see, for example, [26–29] for a review). Khonsary and Calvez [30,31] introduced the description of lesion formation that considers species' spatial distribution. The authors formulated a model based on partial differential equations (PDEs) to reproduce the concentric demyelinating rings observed in type III MS/Balò sclerosis. Following the immunopathological findings on type III MS/Balò sclerosis, they assumed that activation of innate immunity by an unknown pathogen was responsible for initiating the inflammatory cascade, leading to the destruction of oligodendrocytes. Their system describes the spatiotemporal dynamics of immune cells, chemical mediators, and damaged oligodendrocytes. Moving from [30,31], in [32–35], the authors took into account the macrophage production of cytokines and, through theoretical and numerical bifurcation analysis, were able to reproduce several pathological scenarios observed in type III MS/Balò sclerosis. Recently, in [36], they have considered an Allee-type growth term to reproduce macrophage activation and studied the effect on the illness progression. Moise and Friedman [12] have proposed a comprehensive spatial model. The authors also analyzed the impact of specific drugs for MS treatment and compared their findings with clinical data. The model encompasses multiple species' interactions to replicate MS's intricate biological pathways with remarkable detail. However, the mathematical complexity makes the system unsuitable for analytical analysis, and the results heavily rely on numerical simulations. This does not allow for an understanding of the fundamental mechanisms leading to the different illness scenarios, nor to elucidate which are the key parameters guiding the progression and transition of the pathology. Finally, through an Ordinary Differential Equation-Partial Differential Equation (ODE–PDE) system, the interplay between the adaptive and immune responses in the development of MS is elucidated, [37].

1.3. Aims of the paper

This paper aims to derive a model incorporating the influence of cytokines on macrophage activation. In [33], the kinetic term reproducing proliferation of activated macrophages is a logistic functional form whose constant activation rate describes the effect of an unknown antigen directly acting on resident immune cells. This mechanism reproduces the findings of many immunopathological studies (see [16,20,21,38]), which report activation of macrophages in the absence of cytokine-driven regulatory effects. Experimental models, such as the induction of type III lesions through lipopolysaccharide injection into rats' spinal cords, confirm direct macrophage activation without cytokine involvement, leading to focal areas of microglial activation and oligodendrocyte apoptosis [21]. Despite various hypotheses proposed to elucidate the triggering factors of the immune response, such as CNS antigens in MS or the Epstein–Barr virus, no study has definitively identified the antigen or provided a universally accepted explanation for the activation mechanism to date [39]. In fact, some studies suggest that inflammatory cells, exhibiting a cytokine-producing phenotype, are already present in the early stages of lesions, potentially initiating a pathogenic cascade of events leading to demyelination and oligodendrocyte damage [21,40,41]. Considering that the medical literature predominantly recognizes cytokines as the primary chemical mediators

driving inflammatory activation in MS [42], these findings lead to the hypothesis of the involvement of cytokines in the activation process. Moreover, mathematical descriptions of MS and inflammation-driven diseases typically consider cytokine participation in the proliferation of activated macrophages [12,23,25]. The primary goal of this paper is to test the hypothesis regarding cytokine-mediated activation of the immunopathological response in MS. Therefore, we modify the activation rate in the macrophage equation of the model in [33] by choosing a logistic functional form with a cytokine-dependent growth rate that displays Holling-type saturation at high cytokine concentrations. The modified form of the kinetics describes a more general scenario of [33], which is recovered in the limit of vanishingly small values of the newly introduced half-saturation parameter of the growth rate. Moreover, since some of the currently used immunomodulatory drugs for the treatment of MS inhibit cytokine production and T-cell proliferation, by varying the value of the cytokine half-saturation constant, we could mimic the effect of medical treatment on disease dynamics and investigate its impact on the lesions.

We focus on the study of the Turing-type instabilities of the nontrivial homogeneous steady state, leading to the settlement of stationary patterns of inflammation and demyelination. At the onset of the instability, we carry out the linear and weakly nonlinear analysis which yield quantitative estimates of the most relevant pattern properties, such as bifurcation threshold, wavelength, amplitude, and form. We analyze how the emergent pattern changes by varying the parameters within experimentally estimated ranges, especially focusing on the effects of varying the cytokine half-saturation constant. We find that the involvement of cytokines in the proliferation of macrophages results in a less aggressive form of the disease and in a slower progression of the inflammation compared to the case of direct activation of the innate immune system.

In the paper's final part, we examine the proposed model's well-posedness. The mathematical properties of chemotactic-diffusion-reaction systems, initially introduced by Keller and Segel, have been extensively studied [43–47]. It is also well-known that aggregation of cells may lead to blow-up phenomena [48]. Well-posedness of the considered model depends on the form of the chemotactic term and on the presence of reproduction and saturation kinetic terms. If one introduces volume-filling effects in the chemotaxis term, global existence and uniqueness of the solutions to the Cauchy problem can be proved [49]. Moreover, the inclusion of logistic-type kinetics and/or growth limitations on the sensitivity function prevents blow-up of the solutions [50,51].

The well-posedness of the system proposed in [33] has been studied in [52–54], where the authors prove the existence and uniform-in-time boundedness of strong solutions. If porous media-type nonlinear diffusion terms are included, the existence of global weak solutions is shown in [55]. Indeed, the results obtained in [52,54] hold also for the model presented in the present paper. Therefore, in this paper, we consider the mathematically interesting case when the production mechanism of activated macrophages has no saturation effects as the density of the cytokine increases. This scenario is recovered from the kinetics presented here in the limit of large values of both the half-saturation constant and the constant growth rate. In the absence of cytokine-induced growth-limiting effects, we prove the existence of a unique, strong solution that exists globally in time.

1.4. Plan of the paper

The paper is organized as follows: in Section 2 we present the model. In Section 3, we perform a Turing stability analysis at the onset of the stationary bifurcation and derive the explicit expressions of the critical value of the chemotactic coefficient and the critical wavenumber of the pattern. In Section 4, we discuss the parameter values adopted in the analysis, either taken from experimental literature or estimated. In Section 5 we perform a weakly nonlinear analysis on 1D spatial domains and obtain the amplitude equation that captures the dynamics of the system close to criticality. We also derive the Ginzburg–Landau equation that describes the wave-like invasion of the pattern through the domain. Section 6 provides a detailed numerical investigation of dynamics supported by the proposed model on 2D spatial domains. In Section 7, we prove global in-time well-posedness of the model, when the reaction kinetics of the activated macrophages have no saturation effects. In Section 8, we finally draw some conclusions and discuss open problems.

2. Mathematical model for MS lesions formation

The mathematical model we propose aims to reproduce the formation of MS lesions by the interaction of three species: immune cells namely activated M1 macrophages or activated microglia, cytokines, and oligodendrocytes. Let $\tilde{m}(T,X)$, $\tilde{c}(T,X)$ and $\tilde{d}(T,X)$ be the densities of macrophage, cytokine, and oligodendrocyte species, respectively, where $(T,X)\in\mathbb{R}^+\times\Omega$, with $\Omega\subset\mathbb{R}^n$, $n=1,2$ is a bounded domain on which we impose no-flux boundary conditions. Our model is a generalization of the model proposed in [33], which describes the initial stages of the disease leading to type-III lesions, characterized by macrophage activation by innate immunity, high levels of oligodendrocyte apoptosis, and minimal or absent lymphocyte infiltration [16,18,20,21]. Here, we generalize the model proposed in [33] to include the involvement of the cytokines in the activation of immune cells. We therefore introduce the following system of PDEs:

$$\begin{cases} \dfrac{\partial\tilde{m}}{\partial T} = D\Delta_{\mathbf{X}}\tilde{m} - \nabla_{\mathbf{X}}\cdot(\Psi(\tilde{m})\nabla_{\mathbf{X}}\tilde{c}) + \lambda\dfrac{\tilde{c}}{k_{\tilde{c}}+\tilde{c}}\tilde{m}(\overline{m}-\tilde{m}), \\ \dfrac{\partial\tilde{c}}{\partial T} = \dfrac{1}{\nu}(\varepsilon\Delta_{\mathbf{X}}\tilde{c} + \mu\tilde{d} + b\tilde{m} - \alpha\tilde{c}), \\ \dfrac{\partial\tilde{d}}{\partial T} = \kappa\, F(\tilde{m})\,\tilde{m}\,(\overline{d}-\tilde{d}), \end{cases} \tag{2.1}$$

with $\Psi(\tilde{m}) = \psi\frac{\tilde{m}}{\overline{m}+\tilde{m}}$ and $F(\tilde{m}) = \frac{\tilde{m}}{\overline{m}+\tilde{m}}$. Since microglia and macrophages express similar molecular markers and are often experimentally indistinguishable [8], we shall represent them as a single species. The spatial movement of macrophages is described by diffusion and chemotaxis: the diffusion term $D\Delta_{\mathbf{X}}\tilde{m}$ accounts for the random movement of cells, where $\Delta_{\mathbf{X}} = \nabla_{\mathbf{X}}\cdot\nabla_{\mathbf{X}}$, $\nabla_{\mathbf{X}} = \partial/\partial\mathbf{X}$ and D is the constant diffusion rate. Following [33], we describe the chemotactic movement of the cells by a density-dependent chemotactic sensitivity function $\Psi(\tilde{m})$, which displays saturation of chemotaxis due to overcrowding effects, where ψ is the maximum chemotactic rate and $\overline{m}$ is the characteristic density of resident (non-activated) cells.

The kinetic term describes the production rate of activated macrophages/microglia $\tilde{m}$ and represents the novelty of the present model with respect to [33]. The model presented in [33] describes the onset of plaque formation in type III and Baló sclerosis, which, according to many studies, is characterized by direct activation of the innate immune response (macrophages/microglia) by an unknown pathogen, in the absence of cytokine-driven regulatory effects [16,20,21,38]. Without going into the details of the activation process, in [33] the macrophage production term is therefore modeled by a logistic function of $\tilde{m}$, namely $\lambda\tilde{m}(\overline{m}-\tilde{m})$, to reproduce production of the activated cells at a constant growth rate λ, and saturation at the average density of resident non-activated macrophages $\overline{m}$. The same functional form has been used in similar models of MS [30,31] and in ODE models of acute inflammation [23]. In the model, the effect of the unknown pathogen responsible for initiation of MS is reproduced by choosing an initial condition consisting of a localized bump of activated macrophages in the absence of signaling molecules and damaged oligodendrocytes. However, other data suggest that pro-inflammatory cytokines are responsible for the inflammatory cascade, ultimately leading to demyelination [40–42]. Hence, in this paper, we want to generalize the model in [33] to include the role played by the pro-inflammatory cytokines to the activation of macrophage/microglia. To describe the activation of macrophages mediated by cytokines

we choose a logistic-type functional form with a cytokine-dependent growth rate $\lambda(c) = \lambda\frac{\tilde{c}}{k_{\tilde{c}}+\tilde{c}}$, where $k_{\tilde{c}}$ is the cytokine half-saturation constant. A similar term was used in [12]. Although different cytokine species stimulate the proliferation of activated macrophages and promote chemotaxis, we do not distinguish between different mediators and indicate by $\tilde{c}(T,\mathbf{X})$ any type of pro-inflammatory signaling cytokines.

Note that the model in [33] derives from (2.1) by setting $k_{\tilde{c}} = 0$. Since for any $k_{\tilde{c}} > 0$, the saturation effect slows down the rate of macrophage activation, the variation of the newly introduced parameter $k_{\tilde{c}}$ affects the time of plaque formation.

The equation for the evolution of $\tilde{c}$ is the same as in [33]: the cytokines diffuse in space with diffusivity coefficient ϵ, and damaged oligodendrocytes release them and activated macrophages with linear kinetics, whose coefficients are μ and b, respectively and they linearly decay at a constant rate α. Finally, the parameter ν measures the characteristic time scale of the cytokine dynamics (see [33]).

The oligodendrocyte equation is as in [30,31,33]: the destroyed oligodendrocytes are immotile, so no spatial term is included. $\overline{d}$ indicates the initial characteristic density of healthy oligodendrocytes in the brain: intact oligodendrocytes are destroyed by interaction with activated macrophages through a mass action law with a coefficient that is a nonlinear saturating function of macrophage density and whose strength is measured by the parameter κ.

We now introduce the following non-dimensional variables and parameters:

$$m = \frac{\tilde{m}}{\overline{m}}, \quad d = \frac{\tilde{d}}{\overline{d}}, \quad c = \frac{\alpha}{\overline{b}\overline{m}}\tilde{c}, \quad t = \lambda\overline{m}T, \quad \mathbf{x} = \sqrt{\frac{\lambda\overline{m}}{D}}\mathbf{X},$$
$$\chi = \frac{\psi\overline{b}}{\alpha D}, \quad \tau = \frac{\nu\lambda\overline{m}}{\alpha}, \quad \epsilon = \frac{\varepsilon\lambda\overline{m}}{\alpha D}, \quad \beta = \frac{b}{\overline{b}}, \quad r = \frac{\kappa}{\lambda}, \tag{2.2}$$
$$\delta = \frac{\mu\overline{d}}{\overline{m}\overline{b}}, \quad \xi = \frac{\alpha k_{\tilde{c}}}{\overline{b}\overline{m}}$$

where all the non-dimensional variables and parameters are as in [33], except ξ: this is the new parameter that rules the effect of cytokines on the macrophage activation rate. Then, the system (2.1) assumes the following non-dimensional form:

$$\begin{cases} \dfrac{\partial m}{\partial t} = \Delta m - \nabla\cdot(\chi(m)\nabla c) + \dfrac{c}{\xi + c}\, m(1-m), & (x,t)\in\Omega_T \\ \dfrac{\partial c}{\partial t} = \dfrac{1}{\tau}\left(\epsilon\Delta c + \delta d - c + \beta m\right), & (x,t)\in\Omega_T \\ \dfrac{\partial d}{\partial t} = rF(m)\, m\,(1-d), & (x,t)\in\Omega_T \end{cases} \tag{2.3}$$

with $\chi(m) = \chi\frac{m}{1+m}$, $F(m) = \frac{m}{1+m}$, $\Omega_T = (0,T)\times\Omega$, where Ω is a bounded domain in $\mathbb{R}^n$ ($n\in\mathbb{N}$, $n\geq 1$) with smooth boundary $\partial\Omega$ on which no-flux (homogeneous von Neumann) boundary conditions are imposed. Moreover, we shall impose the following conditions on the parameters:

$$\chi > 0, \quad \tau > 0, \quad \epsilon > 0, \quad \beta \geq 0, \quad r > 0, \quad \delta \geq 0, \quad \xi \geq 0. \tag{2.4}$$

We are interested in investigating the effects of the new term $c/(\xi + c)$ on the formation of aggregates and compare the results with those obtained in the case $\xi = 0$, which yields the model in [33].

3. Turing instability analysis

In this Section, we conduct a linear stability analysis of system (2.3) to explore the formation of small-amplitude stationary structures emerging from a Turing instability of the non-trivial homogeneous equilibrium. The system (2.3) admits two spatially uniform steady states, namely the disease-free equilibrium $P_0 = (0,0,0)$ and the point $P^* = (m^*, c^*, d^*) = (1, \beta+\delta, 1)$. As in [33], the equilibrium P_0 is unstable while P^* is a stable, attractive node with respect to spatially uniform perturbations for all values of the parameters satisfying (2.4).

The linearized dynamics of (2.3) in the neighborhood of the steady state P^* reads:

$$\dot{\mathbf{w}} = J'\mathbf{w} + D'\Delta\mathbf{w}, \tag{3.1a}$$

where:

$$\mathbf{w} = \begin{pmatrix} m-m^* \\ c-c^* \\ d-d^* \end{pmatrix}, \qquad J' = \begin{pmatrix} -\theta & 0 & 0 \\ \frac{\beta}{\tau} & -\frac{1}{\tau} & \frac{\delta}{\tau} \\ 0 & 0 & -\frac{r}{2} \end{pmatrix}, \tag{3.1b}$$

$$\theta = \frac{\beta+\delta}{\xi+\beta+\delta}, \qquad D' = \begin{pmatrix} 1 & -\frac{\chi}{2} & 0 \\ 0 & \frac{\epsilon}{\tau} & 0 \\ 0 & 0 & 0 \end{pmatrix}. \tag{3.1c}$$

We note that, under the assumptions (2.4), the parameter θ can be written as:

$$\theta = \frac{c^*}{\xi + c^*}, \qquad \text{so that} \qquad 0 \leq \theta < 1 \qquad \text{and} \qquad \theta|_{\xi=0} = 1, \tag{3.2}$$

where $c^* = \beta + \delta$ is the constant equilibrium value of the cytokines. We observe that for $\xi = 0$, one recovers the model presented in [33], which therefore corresponds to $\theta = 1$. For this reason, hereafter, we shall indicate all the quantities evaluated for the model given in [33] with the subscript (1). We also remark that the only difference with the linearized kinetics of the model proposed in [33] is in the coefficient $J'_{(1,1)}$ of the matrix J', where the linearized kinetics of [33] is obtained from (3.1a)–(3.1c) by setting $\theta = 1$.

We now look for solutions of Eq. (3.1a) of the form $\mathbf{w} \propto e^{\sigma t + i\mathbf{k}\cdot\mathbf{x}}$, where σ is the linear growth rate of the Fourier mode of the perturbation with wavenumber $\mathbf{k}$. Since we are imposing no-flux boundary conditions on the spatial domain $\Omega = [0,\ell]$, the wavenumbers admitted by the boundary conditions must be of the form $|\mathbf{k}| = n\pi/\ell$, with $n\in\mathbb{Z}$. Substituting in (3.1a), we get a cubic equation for the eigenvalues, which easily gives one eigenvalue equal to $-r/2$. We then obtain the following dispersion relation, which gives the eigenvalue σ as a function of the wavenumber $k = |\mathbf{k}|$:

$$\sigma^2 + g(k^2)\sigma + h(k^2) = 0, \tag{3.3a}$$

where:

$$g(k^2) = k^2 tr(D) - tr(J), \tag{3.3b}$$
$$h(k^2) = det(D)k^4 + qk^2 + det(J), \tag{3.3c}$$
$$q = \frac{2(1+\theta\epsilon) - \chi\beta}{2\tau}, \tag{3.3d}$$

and

$$J = \begin{pmatrix} -\theta & 0 \\ \frac{\beta}{\tau} & -\frac{1}{\tau} \end{pmatrix}, \qquad D = \begin{pmatrix} 1 & -\frac{\chi}{2} \\ 0 & \frac{\epsilon}{\tau} \end{pmatrix}. \tag{3.3e}$$

For Turing instability to occur, the steady state must be stable in the absence of spatial effects (*i.e.*, $\mathrm{Re}\{\sigma(k^2=0)\} < 0$), and it must be linearly unstable with respect to spatial disturbances. Namely it must exist $k \neq 0$ such that $\mathrm{Re}\{\sigma(k^2)\} > 0$. From (3.3d)–(3.3e), one can easily see that $g(k^2) > 0\ \forall k$. Therefore, the only possibility for Eq. (3.3a) to have a positive root is that $h(k^2) < 0$ for some nonzero k, see [56]. Since $h(k^2)$ is a concave-up parabola, a nonzero k exists such that $h(k^2) < 0$ only if its minimum is negative. The minimum of h is attained at

$$k^2 = -\frac{q}{2\det D} \equiv k_c^2. \tag{3.4}$$

where k_c denotes the critical wavenumber, corresponding to the most unstable mode. The expression (3.4) requires $q < 0$, which is satisfied by imposing the following necessary condition:

$$\chi > \overline{\chi} := \frac{2(1+\theta\epsilon)}{\beta}. \tag{3.5}$$

Marginal stability is obtained for $h(k_c^2) = 0$, so that the bifurcation value χ_c can be found by requiring:

$$\min_k(h(k^2)) = 0, \tag{3.6}$$

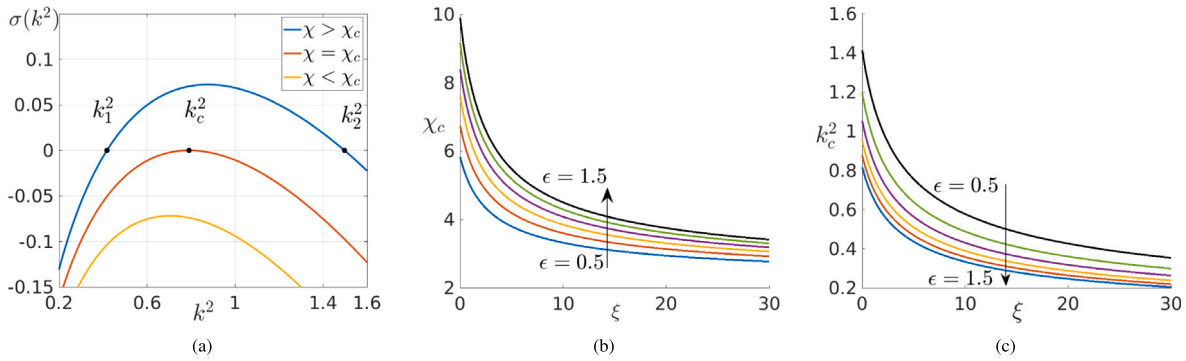

Fig. 1. (a) Plot of the growth rate $\sigma(k^2)$ as a function of k^2 for different values of the bifurcation parameter χ. For $\chi > \chi_c$ there exists a range $[k_1^2, k_2^2]$ for which $\sigma(k^2) > 0$. At $\chi = \chi_c$, $\sigma(k_c^2) = 0$ while $\sigma(k^2) < 0$ elsewhere. For $\chi < \chi_c$, $\sigma(k^2) < 0\ \forall k > 0$. (b) Plot of the critical value χ_c as a function of ξ. The different curves are obtained for evenly spaced values of ϵ in the interval $[0.5, 1.5]$. The other parameters are chosen equal to 1. (c) Plot of k_c^2 as function of ξ. The different curves are obtained for evenly spaced values of ϵ in the interval $[0.5, 1.5]$. The other parameters are chosen equal to 1.

Eq. (3.6) can be solved substituting (3.4) in the expression of $h(k^2)$ given by (3.3d). The bifurcation value is finally given by:

$$\chi_c = \frac{2}{\beta}\left(1 + \sqrt{\theta\epsilon}\right)^2. \tag{3.7}$$

Using the expression of χ_c in (3.4), we obtain the corresponding critical wavenumber:

$$k_c^2 = \sqrt{\frac{\theta}{\epsilon}}. \tag{3.8}$$

For the Turing instability to occur, it has to be $\min_k(h(k^2)) < 0$, which leads to $\chi > \chi_c$. Observing that $\chi_c \geq \overline{\chi}$, so that (3.5) is satisfied if $\chi > \chi_c$, one has the proof of the following theorem.

Theorem 3.1 (*Turing Instability*). *Let the reaction–diffusion system* (2.3) *be given. Then, under the hypotheses* (2.4) *on the parameters, there exists* χ_c, *given by* (3.7), *such that at* $\chi = \chi_c$ *the uniform steady state solution* $(m^*, c^*, d^*) = (1, \beta + \delta, 1)$ *undergoes a Turing bifurcation.*

Remark 3.2. Theorem 3.1 guarantees that there exists a unique value χ_c such that:

i. for $\chi = \chi_c$
- $\sigma(k_c) = 0$, *i.e.* the growth rate $\sigma(k_c)$ of the critical wavenumber k_c is zero;
- $\sigma(k) < 0,\ \forall k \neq k_c$, *i.e.* the growth rate of all the wavenumbers except k_c is negative;

ii. for $\chi - \chi_c > 0$ sufficiently small, there exists a band of wavenumbers $k \in (k_1, k_2)$ such that:
- $\sigma(k) > 0$ for $k \in (k_1, k_2)$, $\sigma(k) < 0$ for $k \notin [k_1, k_2]$, and $\sigma(k_1) = \sigma(k_2) = 0$; *i.e.*, only the wavenumbers belonging to the interval (k_1, k_2), have positive growth rate;
- on the spatial domain $\Omega = [0, \ell]$, if there exist $k \in (k_1, k_2)$ such that $k = n\pi/\ell$, with $n \in \mathbb{Z}$, then the system (2.3) admits a spatially non-homogeneous stationary solution; *i.e.*, the pattern will develop if, within the interval (k_1, k_2), at least one wavenumber is compatible with the no-flux boundary conditions.

Fig. 1(a) shows some graphs of the growth rate $\sigma(k^2)$ for different values of the chemotaxis strength χ, which plays the role of the bifurcation parameter. Comparing these results with those obtained in [33], we observe that $\chi_c \leq \chi_{c_{(1)}}$, which means that the model presented here, compared to the model in [33], admits a lower threshold of the chemotactic coefficient to have the Turing instability. Therefore, the contribution of cytokines to the macrophage proliferation rate allows for the onset of aggregates of inflammation at lower levels of aggressiveness compared with the direct activation of the innate immunity described by [33]. Moreover, we find $k_c \leq k_{c_{(1)}}$. Namely, the critical wavenumber prescribed by the present model is lower than that found in [33]. This means that, in the presence of a cytokine-mediated activation of macrophages, the characteristic size of the plaques and their spacing are larger. We finally note that the explicit expressions of χ_c and k_c depend, through the parameter θ, on the equilibrium value $c^* = \beta + \delta$ of the cytokines, which, in the present model, directly influences the critical threshold of the chemotactic parameter and the critical wavenumber of the emerging pattern.

In Figs. 1(b)–1(c) we display the graphs of χ_c and k_c^2 versus ξ for various values of ϵ. As discussed above, the plots show that χ_c and k_c^2 are monotonously decreasing functions of ξ. Additionally, increasing the value of ϵ, which is proportional to the species' diffusivity ratio has a stabilizing effect on the homogeneous equilibrium. This effect is evident from the fact that, for any fixed value of ξ, the critical value of χ is larger as ϵ grows. Correspondingly, once the pattern has formed, its characteristic size is larger if one increases the diffusivities ratio, as indicated by the fact that, for any fixed ξ, k_c^2 is smaller as ϵ grows.

4. Parameter values

The numerical values or the ranges for the parameters introduced in the system (2.1) are determined or estimated in [33], derived from previous experimental estimates and recent studies [30,57]. We need only to determine the numerical value of the cytokine half-saturation constant, $k_{\bar{c}}$, that we have introduced here.

The functional dependence we propose in (2.1) for the macrophage production rate is based on the model presented in [12] for the activation of the pro-inflammatory M1 immune cells: it is of logistic type with a cytokine-dependent growth rate $\lambda(c) = \lambda\frac{\bar{c}}{k_{\bar{c}}+\bar{c}}$, where $k_{\bar{c}}$ is the cytokine half-saturation constant. In [12], the activation of the macrophages M1 is favored by the presence of cytokines I_{17}, I_{23}, S (see eq. (2.9) in [12]). Therefore, to estimate the range of physiologically meaningful numerical values for $k_{\bar{c}}$, we focus on the steady-state densities of I_{17}, I_{23}, S cytokines (see Table 3 of [12]). We note that I_{23} cytokines are moderately effective, as they assume, at the steady state, an intermediate value of the density among the three different types of cytokines considered. Therefore, we refer to I_{23} to estimate $k_{\bar{c}}$. Differently from the procedure followed in [12], where some assumptions are made, we take the value of the concentration of activated I_{23} (*i.e.* in plaques) as given in [11], namely 250 pg/ml:

$$I_{23}^0 = 250\frac{\text{pg}}{\text{ml}} = 0.25\frac{\text{pg}}{\text{mm}^3} \tag{4.1}$$

Following [12], the value of the half-saturation coefficient $k_{I_{23}}$ is derived assuming the Michaelis–Menten formula, namely $I_{23}^0/(k_{I_{23}} + I_{23}^0) = 5/6$. It therefore follows that:

$$k_{I_{23}} = \frac{I_{23}^0}{5} \tag{4.2}$$

Table 1
Dimension carrying parameter values of the model.

Parameter	Description	Value	Source
$\bar{m}$	average macrophages density	350 cells mm^{-2}	[58]
$\bar{d}$	average oligodendrocyte density	400 cells mm^{-2}	[59]
λ	macrophages activation rate	$\sim 3\cdot 10^{-6}$ mm^2 cells^{-1} min^{-1}	Estimated
D	macrophages random motility	$6.6\cdot 10^{-5}$ mm^2 min^{-1}	[60]
ψ	chemoattraction	0.0023–0.298 mm^2 min^{-1} cells pg^{-1}	Derived from [60]
ϵ/ν	cytokine diffusion	$9\cdot 10^{-4}$ mm^2 min^{-1}	[61]
b/ν	cytokine production rate	$5.7\cdot 10^{-6}$–$1.96\cdot 10^{-5}$ pg min^{-1} cells^{-1}	[62,63]
μ/ν	cytokine production rate per oligodendrocyte	10^{-6}–10^{-5} pg min^{-1} cells^{-1}	Estimated
α/ν	cytokine decay rate	0.001–0.03 min^{-1}	[63]
κ	damaging intensity	$3.96\cdot 10^{-6}$ mm^2 cells^{-1} min^{-1}	[30]
$k_{\bar{c}}$	cytokines half-saturation coefficient	0.136 pg^{-1}mm^{-2}	[11,12]

Table 2
Non dimensional parameter values used in the numerical simulations.

Parameter	Description	Value
χ	chemoattraction	4–55
τ	time scale of cytokine dynamics	0.001–1
ϵ	cytokine diffusion	0.5–1.5
β	cytokine production rate	0.2–1
δ	cytokine production rate per oligodendrocyte	0–1
r	damaging intensity	0.01–6
ξ	cytokine half-saturation coefficient	0.02–0.6

The value of $k_{I_{23}}$ on 3D spatial domains is then given by $k_{\bar{c}_{3D}} = k_{I_{23}} = I^0_{23}/5 = 0.05\,\text{pg/mm}^3$. On 2D domains we have $k_{\bar{c}_{2D}} = (k_{\bar{c}_{3D}})^{2/3} = 0.136\,\text{pg/mm}^2$.

In Table 1, we summarize the physiologically meaningful values for the entire set of parameters along with the corresponding units and descriptions.

From the above scaling, we derive the admissible values for the dimensionless parameter ξ as given in (2.2) and use them in the numerical simulations.

$$\xi_{min} = \frac{k_{\bar{c}}\cdot\frac{\alpha}{\nu_{min}}}{\frac{\bar{b}}{\nu}\cdot\bar{m}} = \frac{0.136\cdot 10^{-3}}{1.96\cdot 10^{-5}\cdot 3.5\cdot 10^{2}} = 0.0198 \tag{4.3a}$$

$$\xi_{max} = \frac{k_{\bar{c}}\cdot\frac{\alpha}{\nu_{max}}}{\frac{\bar{b}}{\nu}\cdot\bar{m}} = \frac{0.136\cdot 3\cdot 10^{-2}}{1.96\cdot 10^{-5}\cdot 3.5\cdot 10^{2}} = 0.5948 \tag{4.3b}$$

So that $\xi_{2D}\in[0.02, 0.6]$.

On 1D spatial domains one has: $k_{\bar{c}_{1D}} = (k_{\bar{c}_{3D}})^{1/3} = 0.368$ pg/mm, and $\bar{m}_{1D} = (\bar{m}_{2D})^{1/2} = 18.7$ *cells/mm*, so that $\xi_{1D}\in[1, 30]$.

Table 2 shows the range of values for the entire set of dimensionless parameters that we shall use for the simulations on 2D spatial domains.

5. Pattern formation on 1D domain

In this Section, we construct spatially non-constant solutions of (2.3) arising from the Turing instability. To this end, through the multiple scales method, we derive the amplitude equations for the spatially periodic solutions to the system (2.3) on the 1D spatial domain $\Omega = [0, \ell]$. Specifically, in Section 5.1, we derive the Stuart–Landau equation that governs the characteristics of small-amplitude stationary patterns. In Section 5.2, we obtain the Ginzburg–Landau equation, which describes the wave-like propagation of the pattern through the domain.

5.1. Weakly nonlinear analysis

Adopting the formalism of [64–67], we perform a weakly nonlinear analysis close to the uniform steady state $P^* = (m^*, c^*, d^*) = (1, \beta+\delta, 1)$.

We set a small control parameter $\eta^2 = (\chi - \chi_c)/\chi_c$, which gives the dimensionless distance of χ from the bifurcation value χ_c. Upon translation of the equilibrium P^* to the origin, the system (2.3) can be written as:

$$\frac{\partial \mathbf{w}}{\partial t} = \mathcal{L}^{\chi}\mathbf{w} + \mathcal{N}\mathbf{w}, \tag{5.1}$$

where $\mathbf{w}$ is defined in (3.1b), the linear operator $\mathcal{L}^{\chi} = J' + D'(\chi)\partial_{xx}$ with J' and D' defined in (3.1b), and $\mathcal{N}$ is a nonlinear operator containing higher order powers in $\mathbf{w}$. Close to equilibrium we expand $\mathbf{w}$ and the bifurcation parameter χ as follows:

$$\mathbf{w} = \eta\,\mathbf{w}_1 + \eta^2\mathbf{w}_2 + \eta^3\mathbf{w}_3 + O(\eta^4),$$
$$\chi = \chi_c + \eta^2\chi_2 + O(\eta^4),$$

and look for solutions having a multiple scale dependence on time t:

$$\mathbf{w}_i = \mathbf{w}_i(T_2, T_4, \ldots),$$

where

$$T_2 = \eta^2 t, \quad T_4 = \eta^4 t, \ldots.$$

so that the time derivative operator has the following expansion:

$$\frac{\partial}{\partial t} = \eta^2\frac{\partial}{\partial T_2} + \eta^4\frac{\partial}{\partial T_4} + O(\eta^5).$$

We introduce the following notation: $\mathbf{w}_i = (w_{m_i}, w_{c_i}, w_{d_i})^T$ $(i = 1, 2\ldots)$, and:

$$\Xi(m) = \frac{m}{1+m}, \qquad \Phi(m, d) = \frac{m^2}{1+m}(1-d).$$

By substitution of the above expansions into (5.1) and collecting the terms at each order in η, we obtain the following systems:

$$O(\eta): \quad \mathcal{L}^{\chi_c}\mathbf{w}_1 = \mathbf{0}, \tag{5.2a}$$

$$O(\eta^2): \quad \mathcal{L}^{\chi_c}\mathbf{w}_2 = \mathbf{F}, \tag{5.2b}$$

$$O(\eta^3): \quad \mathcal{L}^{\chi_c}\mathbf{w}_3 = \mathbf{G}, \tag{5.2c}$$

with $\mathcal{L}^{\chi_c} = J' + D'(\chi_c)\partial_{xx}$ and the expressions for $\mathbf{F}$ and $\mathbf{G}$ are the following:

$$\mathbf{F} = \begin{pmatrix} \theta w^2_{m_1} + \frac{\xi\theta^2}{(\beta+\delta)^2} w_{m_1} w_{c_1} \\ 0 \\ -r\partial_{md}\Phi(m^*, d^*) w_{m_1} w_{d_1} \end{pmatrix} + \chi_c \begin{pmatrix} \Xi'(m^*)\partial_x\left(w_{m_1}\partial_x w_{c_1}\right) \\ 0 \\ 0 \end{pmatrix},$$

$$\mathbf{G} = \frac{\partial \mathbf{w}_1}{\partial T_2}$$
$$+ \begin{pmatrix} 2\theta w_{m_1} w_{m_2} + \frac{\xi\theta^2}{(\beta+\delta)^2}(w_{m_1} w_{c_2} + w_{m_2} w_{c_1} + w^2_{m_1} w_{c_1}) - \frac{\xi\theta^3}{(\beta+\delta)^3} w^2_{c_1} w_{m_1} \\ 0 \\ -r\left[\partial_{md}\Phi(m^*, d^*)\left(w_{m_1} w_{d_2} + w_{m_2} w_{d_1}\right) + \frac{1}{2}\partial_{mmd}\Phi(m^*, d^*) w^2_{m_1} w_{d_1}\right] \end{pmatrix}$$
$$+ \chi_c \begin{pmatrix} \Xi'(m^*)\partial_x\left(w_{m_1}\partial_x w_{c_2} + w_{m_2}\partial_x w_{c_1}\right) + \frac{\Xi''(m^*)}{2}\partial_x\left(w^2_{m_1}\partial_x w_{c_1}\right) \\ 0 \\ 0 \end{pmatrix}$$
$$+ R(\chi_2)\partial_{xx}\mathbf{w}_1,$$

where:

$$R(\chi_2) = \begin{pmatrix} 0 & \chi_2\Xi(m^*) & 0 \\ 0 & 0 & 0 \\ 0 & 0 & 0 \end{pmatrix}.$$

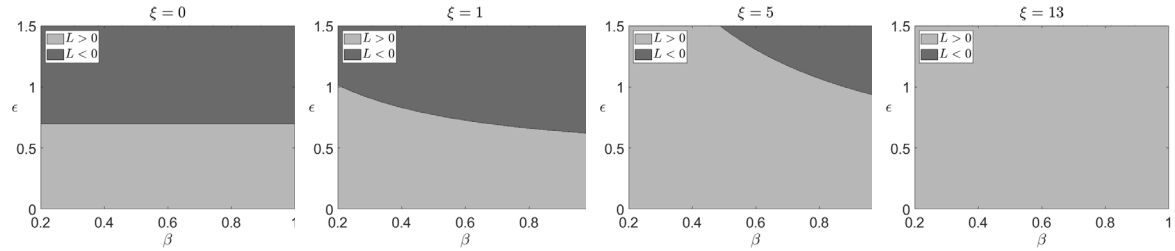

Fig. 2. Turing region: The black bold line corresponds to $L(\epsilon,\beta)=0$. The region in light gray corresponds to the supercritical case $L>0$, whereas the dark gray region corresponds to the subcritical case $L<0$. The parameters are fixed as follows: $\tau=1,\delta=1,r=1,\eta^2=0.1$, with (a) $\xi=0$, (b) $\xi=1$, (c) $\xi=5$ and (d) $\xi=13$. For increasing values of ξ the region corresponding to the subcritical case $L<0$ becomes smaller.

From Eq. (5.2a), by imposing Neumann boundary conditions, one gets a solution of the form:

$$\mathbf{w}_1=\boldsymbol{\rho}A(T_2,\dots)\cos(k_c x),\qquad \boldsymbol{\rho}\in Ker(J'-k_c^2D'(\chi_c)),\tag{5.3}$$

where $A(T_2,\dots)$ is the time-dependent amplitude of the pattern, k_c given by (3.4) must satisfy $k_c=n\pi/\ell, n\in\mathbb{Z}$, and $\boldsymbol{\rho}$ is normalized as follows:

$$\boldsymbol{\rho}=(\rho_1,1,0)=\begin{pmatrix}\frac{1+\epsilon k_c^2}{\beta}\\1\\0\end{pmatrix}.\tag{5.4}$$

By the *Fredholm Alternative theorem*, the solvability condition for the Eq. (5.2b) is given by $\langle\mathbf{F},\boldsymbol{\psi}\rangle=0$, with $\boldsymbol{\psi}\in Ker(\mathcal{L}^*)$, where we have denoted by $\mathcal{L}^*$ the adjoint of $\mathcal{L}^{\chi_c}$ and by $\langle\cdot,\cdot\rangle$ the scalar product in $L^2(0,\ell)$. As before, by imposing Neumann boundary conditions, one gets a solution of the form:

$$\boldsymbol{\psi}=\boldsymbol{\rho}'\cos(k_c x),\qquad \text{where } Ker(\mathcal{L}^*)\ni\boldsymbol{\rho}'=\begin{pmatrix}\frac{\beta}{\tau(k_c^2+\theta)}\\1\\\frac{2\delta}{r\tau}\end{pmatrix}.\tag{5.5}$$

At order η^2 the solvability condition is automatically satisfied and the solution $\mathbf{w}_2$ to the second-order system (5.2b) is given by:

$$\mathbf{w}_2=A^2[\mathbf{w}_{20}+\mathbf{w}_{22}\cos(2k_c x)],\tag{5.6}$$

where the vectors $\mathbf{w}_{2i}=(w_{m_{2i}},w_{c_{2i}},w_{d_{2i}})^T$ for $i=0,2$ are the solutions of the following linear system:

$$\begin{cases}J'\mathbf{w}_{20}=\frac{\theta\rho_1}{2}\left(\rho_1+\frac{\xi\theta}{(\beta+\delta)^2},0,0\right)^T,\\ \left(J'-4k_c^2D'(\chi_c)\right)\mathbf{w}_{22}=\left(\frac{\theta\rho_1}{2}\left(\rho_1+\frac{\xi\theta}{(\beta+\delta)^2}\right)-\rho_1\chi_c k_c^2\Xi'(m^*),0,0\right)^T.\end{cases}\tag{5.7}$$

Substituting $\mathbf{w}_1$ and $\mathbf{w}_2$ into (5.2c), one gets the following expression for $\mathbf{G}$:

$$\mathbf{G}=\left(\frac{\partial A}{\partial T_2}\rho+A\mathbf{G}_{10}^{(1)}+A^3\mathbf{G}_{10}^{(3)}\right)\cos(k_c x)+\mathbf{G}^*,$$

where $\mathbf{G}^*$ can be written as $\mathbf{G}^*=A^3[\mathbf{G}_{31}^{*(3)}\cos(3k_c x)+\mathbf{G}_{13}^{*(3)}\cos^3(k_c x)]$. In the above expression $\mathbf{G}_{31}^{*(3)}$ satisfies the Fredholm solvability condition, while $\mathbf{G}_{10}^{(j)}$ for $j=1,3$ and $\mathbf{G}_{13}^{*(3)}$, whose explicit expression is not reported here, depend on the system parameters. Therefore, imposing the solvability condition at the third order, we get the following Stuart–Landau equation for the amplitude $A(T_2)$:

$$\frac{\partial A}{\partial T_2}=\sigma A-LA^3,\tag{5.8a}$$

where:

$$\sigma=\frac{\langle\mathbf{G}_1^{(1)},\boldsymbol{\rho}'\rangle}{\langle\boldsymbol{\rho},\boldsymbol{\rho}'\rangle},\qquad L=\frac{\langle\mathbf{G}_1^{(3)},\boldsymbol{\rho}'\rangle}{\langle\boldsymbol{\rho},\boldsymbol{\rho}'\rangle},\tag{5.8b}$$

and

$$\mathbf{G}_1^{(1)}=-\mathbf{G}_{10}^{(1)}=\begin{pmatrix}\chi_2k_c^2\Xi(m^*)\\0\\0\end{pmatrix},\tag{5.8c}$$

$$\mathbf{G}_1^{(3)}=\mathbf{G}_{10}^{(3)}+\frac{3}{4}\mathbf{G}_{13}^{*(3)}=\begin{pmatrix}\Sigma\\0\\0\end{pmatrix}.\tag{5.8d}$$

where $\Sigma=2\theta\rho_1\left(w_{m_{20}}+\frac{w_{m_{22}}}{2}\right)+\frac{\xi\theta^2}{(\beta+\delta)^2}\left[\rho_1\left(w_{c_{20}}+\frac{w_{c_{22}}}{2}\right)+w_{m_{20}}+\frac{w_{m_{22}}}{2}+\frac{3}{4}\rho_1^2\right]-\frac{3}{4}\frac{\xi\theta^3}{(\beta+\delta)^3}-\chi_c k_c^2\left[\Xi'(m^*)\left(w_{m_{20}}-\frac{w_{m_{22}}}{2}+\rho_1\frac{w_{c_{22}}}{2}\right)+\frac{1}{8}\rho_1^2\Xi''(m^*)\right]$.

One can verify that the growth rate σ is always positive for all values of the parameters for which one has the Turing instability. Then, the dynamics of the Stuart–Landau Eq. (5.8a) can be divided into two qualitatively different cases, depending upon the sign of the Landau coefficient L: for $L>0$, one has the supercritical case that corresponds to the onset of small-amplitude patterns; for $L<0$ one gets the subcritical case that, close to criticality, yields the settlement of finite amplitude structures. In Fig. 2(a)–(c) we present the curve across which $L(\epsilon,\beta)$ changes its sign for different values of ξ and fixed values of the remaining parameters. The curve $L(\epsilon,\beta)=0$ divides the Turing space into two distinct regions: the region where the pattern forms supercritically (displayed in light gray) and the subcritical region (displayed in dark gray). We note that the bifurcation is subcritical in a portion of the parameter space whose width is maximum for $\xi=0$ and that becomes progressively smaller for growing values of ξ. This analysis reveals that the involvement of cytokines in macrophage activation ($\xi>0$ and large) corresponds, in a large portion of the parameter space, to the onset of a *mild* disease, displaying small levels of inflammation even when the chemotactic effect is strong (*i.e.*, the bifurcation parameter is above the Turing threshold).

Conversely, small values of the parameter ξ correspond, in a large parameter region, to the onset of an aggressive disease that, for high values of χ (namely, $\chi>\chi_c$), leads to the formation of demyelinated bands (or ring-shaped plaques on 2D domains) characterized by high levels of inflammation.

5.2. Traveling wavefront equations

In this Subsection, we study the propagation of patterned MS through the spatial domain as a wave (see also [32]). If the domain size is large compared to the characteristic wavelength of the pattern, a large number of modes can be excited, even for values of the bifurcation parameter very close to the critical threshold. The interaction among the excited modes results in a *slow* modulation-in-space of the pattern amplitude. In order to describe this phenomenon quantitatively, one must, therefore, consider that the solution has both a slow and a fast spatial dependence. One can easily argue that the characteristic length scale of the spatial modulation is $O(\eta^{-1})$. The weakly nonlinear analysis of Section 5.1 needs to be modified to consider the dependence of

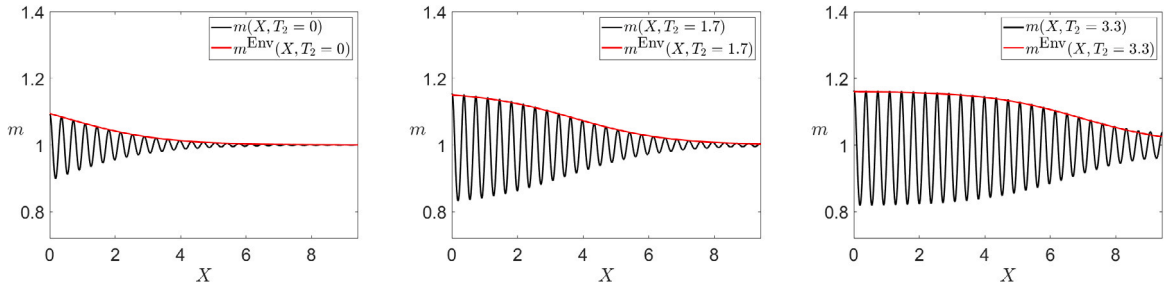

(a) (b) (c)

Fig. 3. The red line represents the envelope m^{Env} of the macrophages solution given by (5.12) as prescribed by the GLE, whose initial condition is depicted in red in Fig. 3(a) and where $A(X,T_2)$ is expressed by (5.11). The black line represents the macrophage numerical solution of the system (2.3) with initial condition $(m_0,c_0,d_0)^T = (m^*,c^*,d^*)^T + \eta A(X,0)\,\boldsymbol{\rho}\cos(\bar{k}_c x)$ reported in black in Fig. 3(a). In Figs. 3(b)–3(c) the two spatial profiles of m^{Env} and of the macrophage numerical solution of the full system (2.3) are displayed at two different times. The parameter values are: $\beta=1$, $\delta=1$, $r=1$, $\tau=1$, $\epsilon=0.5$, $\chi=3.8071$, $\xi=5$. For this set of parameters we obtained $\chi_c=3.7976$, and $\eta=0.05$. (For interpretation of the references to color in this figure legend, the reader is referred to the web version of this article.)

the amplitude A on the slow variable $X=\eta x$. Separating the fast x-dependence and the slow X-dependence and following the same procedure as in Section 5.1, at the leading order in η we recover the homogeneous linear problem $\mathcal{L}_x^{\chi_c}\mathbf{w}_1=\mathbf{0}$, where $\mathcal{L}_x^{\chi_c}$ denotes the operator $\mathcal{L}^{\chi_c}$, defined in Section 5.1 and where we have also emphasized the dependence on the fast spatial variable x. The solution of the first-order equation is:

$$\mathbf{w}_1=\boldsymbol{\rho}\,A(X,T_2,\dots)\cos(k_c x), \tag{5.9}$$

where $\boldsymbol{\rho}$ is given by (5.4).

At the second order in η, we obtain, as in (5.2b), the following linear non-homogeneous problem: $\mathcal{L}_x^{\chi_c}\mathbf{w}_2=\mathbf{F}$. The analytical expression of $\mathbf{F}$ is not reported here; however, as in (5.2b), $\mathbf{F}$ satisfies the Fredholm solvability condition. The solution $\mathbf{w}_2$ of the second-order non-homogeneous system can be recovered as:

$$\mathbf{w}_2=A^2\mathbf{w}_{20}+A^2\mathbf{w}_{22}\cos(2k_c x)+\frac{\partial A}{\partial X}\mathbf{w}_{21}\sin(k_c x),$$

where the vectors $\mathbf{w}_{2i}=(w_{m_{2i}},w_{c_{2i}},w_{d_{2i}})^T$ for $i=0,2$ are the solutions of the linear systems given by (5.7), and $\mathbf{w}_{21}$ is the solution of the following linear system:

$$\left(J'-k_c^2 D'(\chi_c)\right)\mathbf{w}_{21}=2k_c D'(\chi_c)\boldsymbol{\rho}.$$

Substituting the expressions of $\mathbf{w}_1$ and $\mathbf{w}_2$ in the linear problem obtained at the third order, one gets $\mathcal{L}_x^{\chi_c}\mathbf{w}_3=\mathbf{G}$, where $\mathbf{G}$ is expressed as follows:

$$\mathbf{G}=\left(\frac{\partial A}{\partial T_2}\boldsymbol{\rho}+A\mathbf{G}_{10}^{(1)}+A^3\mathbf{G}_{10}^{(3)}+\frac{\partial^2 A}{\partial X^2}\mathbf{G}_{10}^{(0)XX}\right)\cos(k_c x)$$
$$+A\frac{\partial A}{\partial X}\mathbf{G}_{02}^{(1)X}\sin(2k_c x)+\mathbf{G}^*,$$

with $\mathbf{G}^*=A^3[\mathbf{G}_{13}^{*(3)}\cos^3(k_c x)+\mathbf{G}_{31}^{*(3)}\cos(3k_c x)]$, and where $\mathbf{G}_{02}^{(1)X}$ and $\mathbf{G}_{31}^{*(3)}$ satisfy the Fredholm solvability condition. Imposing the solvability condition at the third order, one therefore gets the following Ginzburg–Landau Equation (GLE) for the amplitude $A(X,T_2)$:

$$\frac{\partial A}{\partial T_2}=\nu\frac{\partial^2 A}{\partial X^2}+\sigma A-LA^3 \tag{5.10a}$$

where:

$$\nu=\frac{\langle\mathbf{G}_1^{(0)XX},\boldsymbol{\rho}'\rangle}{\langle\boldsymbol{\rho},\boldsymbol{\rho}'\rangle}, \tag{5.10b}$$

with

$$\mathbf{G}_1^{(0)XX}=-\mathbf{G}_{10}^{(0)XX}=2k_c D'(\chi_c)\mathbf{w}_{21}+D'(\chi_c)\boldsymbol{\rho}, \tag{5.10c}$$

and σ and L are given by (5.8b)–(5.8d).

Choosing the system parameters in such a way that the Landau coefficient L is greater than zero, we can obtain the explicit expression for the solution of the GL Eq. (5.10a), namely:

$$A(X,T_2)=\frac{1}{2}\sqrt{\frac{\sigma}{L}}\left(1-\tanh\left(\sqrt{\frac{\sigma}{\nu}}\frac{z-z_0}{2\sqrt{2}}\right)\right),$$
$$\text{where } z=X-uT_2,\qquad \text{with}\quad u=3\sqrt{\frac{\sigma\nu}{2}}, \tag{5.11}$$

where u is the wave speed, namely the speed of the envelope of the traveling pattern.

In what follows, we shall show some numerical simulations for which we have selected the parameters so that $\chi>\chi_c$ and $L>0$. Precisely, in Fig. 3, we show two curves representing the macrophage species: the envelope of the solution spatial profile as predicted by the GL Eq. (5.10a) (shown by the red line), namely:

$$(m^{\mathrm{Env}},c^{\mathrm{Env}},d^{\mathrm{Env}})^T=(m^*,c^*,d^*)^T+\eta\,A(X,T_2)\,\boldsymbol{\rho}, \tag{5.12}$$

where $A(X,T_2)$ is given by (5.11); and the numerical solution of the system (2.3) (shown by the black line) at different times and for a fixed value of ξ. The initial condition of the solution to (2.3) is a perturbation of the equilibrium P^* localized at the left end side of the spatial domain, precisely $(m_0,c_0,d_0)^T=(m^*,c^*,d^*)^T+\eta A(X,0)\boldsymbol{\rho}\cos(\bar{k}_c x)$, where $\bar{k}_c$ is the first integer or semi-integer allowed by the Neumann boundary conditions that become unstable when χ passes the critical value χ_c (see also [68]). The simulations show that the solution $(m^{\mathrm{Env}},c^{\mathrm{Env}},d^{\mathrm{Env}})^T$ predicted by the GL equation is in good agreement with the amplitude of the numerical solution of the system (2.3) as the wavefront progressively propagates through the domain.

In Fig. 4 we show the envelope of the macrophage solution as predicted by the GL equation and expressed by (5.12), and the numerical solution of the system (2.3) at a fixed time and for different values of ξ. We remark that the critical value of the bifurcation parameter χ_c depends on ξ (see Eq. (3.7)); therefore, as ξ is varied while χ is held fixed, the parameter $\eta=\sqrt{(\chi-\chi_c)/\chi_c}$ also varies, returning for η a monotonically increasing function of ξ. Since for the weakly nonlinear analysis to be valid, we must restrict ourselves to small values of η; this forces us to consider variations of ξ only in a small range. In Fig. 4 we have fixed $\chi=5.8430$; with the chosen parameter set, for $\xi=0$ one gets $\eta=0.05$, while for $\xi=0.15$ one obtains $\eta=0.1807$. Therefore, although with a fixed χ, the three plots in Figs. 4(a)–4(c) are obtained for different values of the distance of χ from the respective bifurcation threshold.

From Fig. 4 we observe that, besides the differences in the pattern wavenumber and the amplitude displayed for different values of ξ, the speed of traveling wavefront invasion seems to change for increasing values of ξ. Therefore, in what follows, we want to investigate how the wavefront velocity depends on ξ. To this aim, upon substituting the expressions of σ and ν, given by (5.8b) and (5.10b), respectively, into

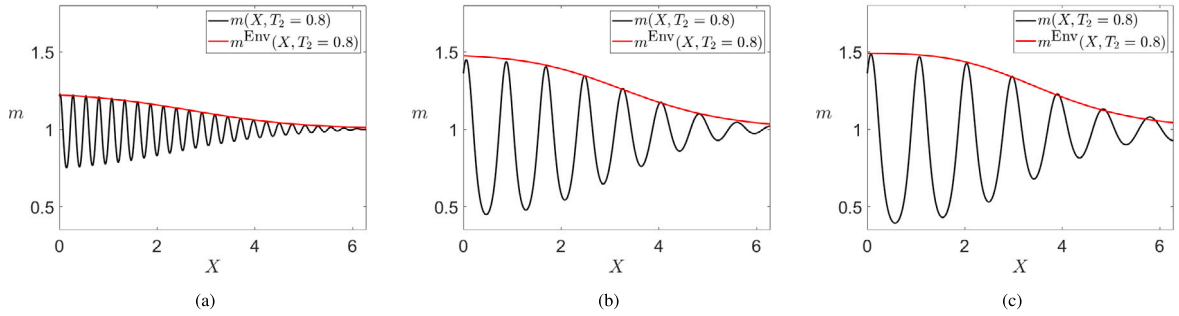

Fig. 4. Traveling wavefront invasion for different values of ξ at the same fixed time T_2. The red line represents the envelope m^{Env} of the macrophages solution prescribed by the GLE as given by (5.12), with the initial condition $A(X,T_2=0)$. The black line represents the macrophage numerical solution of the system (2.3) with initial condition $(m_0,c_0,d_0)^T=(m^*,c^*,d^*)^T+\eta A(X,0)\rho\cos(\bar{k}_c x)$. The parameter ξ is chosen as: (a) $\xi=0$, (b) $\xi=0.1$, (c) $\xi=0.15$. All the other parameter values are: $\beta=1$, $\delta=1$, $r=1$, $\tau=1$, $\epsilon=0.5$, $\chi=5.8430$. (For interpretation of the references to color in this figure legend, the reader is referred to the web version of this article.)

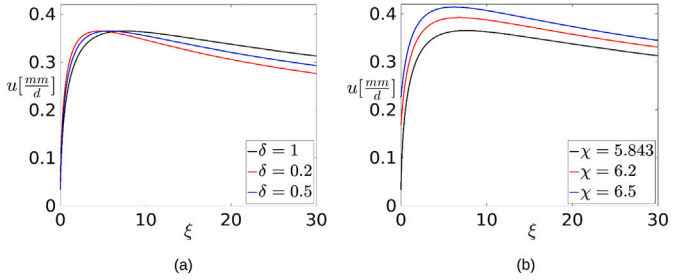

Fig. 5. Plot of the dimension-carrying traveling wavefront invasion speed as a function of the parameter ξ, for fixed values of $\beta=1$, $r=1$, $\tau=1$, $\epsilon=0.5$ and computing $\eta=\sqrt{(\chi-\chi_c)\chi_c}$ for each value of ξ (see text). (a) The different curves are obtained for different values of δ while the value of χ is fixed as $\chi=5.8430$. (b) The different curves are obtained for different values of χ while the value of δ is fixed as $\delta=1$. (For interpretation of the references to color in this figure legend, the reader is referred to the web version of this article.)

the expression of u in (5.11), we derive the explicit dependence of u on ξ (and on the other system parameters). The obtained u is of the form:

$$u(\xi)=\frac{3\sqrt{\epsilon(\beta+\delta)}}{\sqrt{\epsilon(\xi+\beta+\delta)}+\tau\sqrt{\beta+\delta}}, \tag{5.13}$$

resulting in a monotonously decreasing function of ξ, when all the other parameters are held fixed. However, to recover from the expression (5.13) the dimensional velocity (*i.e.*, the one expressed in dimensional units), we have to multiply by a factor that involves the control parameter $\eta=\sqrt{(\chi-\chi_c)/\chi_c}$, which, as we have already noticed, grows with increasing ξ. A typical plot of the resulting traveling wavefront speed expressed in dimensional units as a function of ξ is shown in Fig. 5. We notice that the speed initially grows for increasing ξ while, after a certain threshold, it diminishes as ξ is increased. This behavior can be explained if one considers two different effects that depend on varying ξ: the first is the distance of the bifurcation parameter χ from the critical threshold, and the second is the activation term in the macrophage equation of system (2.3). When ξ is small, the macrophage activation term is close to its maximum value, since $c/(\xi+c)\approx 1$. In this case, keeping a constant value for χ and increasing ξ increases the relative distance between χ and χ_c, which in turn leads to an increasing relative chemotactic strength for the macrophages and to a faster domain invasion for the traveling wavefront. On the other hand, for large values of ξ the activation term for macrophages remains small, due to the high value of the half-saturation constant of the cytokines. In this case, as ξ is increased, the effect of an augmented relative chemotactic strength is overtaken by a lowered activation rate of macrophages, resulting in a slightly decreasing function of ξ for the wavefront invasion speed.

To better illustrate the dependence of the dimensional traveling speed on the parameter ξ, in Fig. 6 we have performed some numerical experiments adopting the following procedure: (1) we have fixed all the parameters, but ξ and χ; (2) for $\xi=0$, we have computed the corresponding value of χ_c and we have performed the simulation fixing $\chi=(1+\eta^2)\chi_c$, with $\eta=0.05$: (3) for each considered value of ξ, we have computed the updated value of χ_c and chosen the value of $\chi=(1+\eta^2)\chi_c$ by keeping the same value of $\eta=0.05$ as in step (2). This procedure allows us to investigate the dependence of the dimensional velocity on ξ maintaining fixed the distance from the bifurcation threshold χ_c as ξ is varied. The corresponding simulations are reported in Fig. 6. We note that, as ξ is increased, keeping the distance of the control parameter from the onset fixed, the wavelength shows only a slight increase with respect to the case $\xi=0$, while the pattern amplitude decreases. This last behavior is opposite to what observed in Fig. 5 (where the value of χ was fixed for different values of ξ, so changing the relative distance from the bifurcation), and is determined by the reduced activation rate of macrophages as ξ increases. In Fig. 7, we show the graph of the dimensional wave velocity computed, holding η fixed, *i.e.*, using the same procedure as in Fig. 6. As expected, since, in this case, the relative distance from the bifurcation threshold does not vary as ξ increases, the only mechanism affecting the wave speed is the inferior activation rate of macrophages, which makes the velocity smaller as ξ is increased.

6. Numerical results on 2D spatial domains

In this Section we present the results of the numerical experiments performed on the system (2.3) on 2D spatial domains. Our aim is to examine the impact on the plaque formation process of the term $c/(\xi+c)$ included the kinetic part of the macrophages equation. We primarily explore how changing ξ and the initial conditions affect the plaque formation process, which is characterized by the emergence of localized zones of apoptotic oligodendrocytes When $\xi=0$, the system has been previously analyzed in [33], which included an extensive sensitivity analysis of the other system parameters under different initial conditions and scenarios. Most of the conclusions regarding the effect of parameter variations for $\xi=0$ remain applicable for $\xi>0$. We refer the interested reader to [33] for further analysis details. All numerical simulations are performed through the spectral solver described in [33].

6.1. Radially symmetric plaques

To examine how $\xi>0$ affects the system, we shall consider an initial configuration comprising of a 0.5 magnitude cytokine cluster, a low concentration (10^{-3}) of uniformly distributed macrophages around the cytokine area, and no oligodendrocytes present. This initial condition creates round-shaped structures in the damaged oligodendrocytes. When $\chi>\chi_c$ satisfies the condition for Turing instability, it produces concentric ring shapes similar to the well-known Baló's sclerosis lesions, as demonstrated in [33]. We fix some of the parameters in the

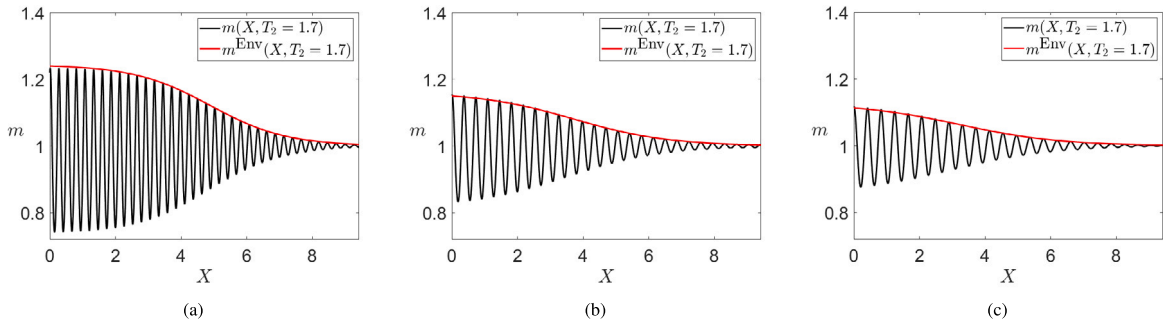

Fig. 6. Comparison of the profiles of the macrophage traveling wave at the same time T_2 for different values of ξ and keeping η fixed as ξ varies (see text). In each figure the red line represents the exact solution of the GLE (5.10a), expressed by (5.11), with the initial condition $A(X,T_2=0)$, while the black line represents the numerical solution of the system (2.3) with initial condition $(m_0,c_0,d_0)^T=(m^*,c^*,d^*)^T+\eta A(X,0)\rho\cos(\bar{k}_c x)$. The parameters are chosen as in Fig. 3 with η fixed as $\eta=0.05$, except for ξ, that is chosen as follows: (a) $\xi=0$, for which one has $\chi=3.5830$; (b) $\xi=5$, for which one has $\chi=3.8071$; (c) $\xi=10$, for which one has $\chi=3.3297$. (For interpretation of the references to color in this figure legend, the reader is referred to the web version of this article.)

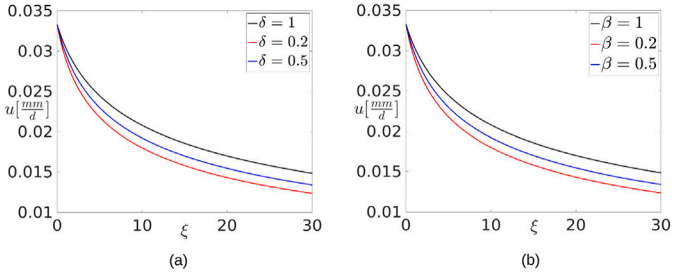

Fig. 7. Plot of the dimension-carrying traveling wavefront invasion speed as a function of the parameter ξ, for fixed values of the other parameters as $r=1$, $\tau=1$, $\epsilon=0.5$, $\eta=0.05$, keeping η fixed as ξ varies and computing $\chi=(1+\eta^2)\chi_c$ for each value of ξ (see text). (a) The different curves are obtained for different values of δ. (b) The different curves are obtained for different values of β. (For interpretation of the references to color in this figure legend, the reader is referred to the web version of this article.)

following way: $\beta=1$ (high cytokine production by macrophages), $\epsilon=0.5$ (low cytokine diffusivity), $\delta=1$ (moderate-high value of the cytokine production by damaged oligodendrocytes), $r=1$ (moderate-low aggressiveness) and $\tau=1$. The parameter ξ varies in the range $[0.01,0.6]$. According to (3.7), for the parameters considered, the critical value χ_c for the emergence of Turing instability ranges in the interval $[5.249,5.872]$ (lower value χ_c corresponds to higher ξ and vice versa).

In our analysis, we utilize specific metrics to quantify the measurement of the radially symmetric plaque. The primary metric, P_{size}, quantifies the area of demyelination resulting from the accumulation of macrophages. Following the method utilized in [16] for Alzheimer's plaques, we define P_{size} at a specific time as the radius of the region where the decrease in destroyed oligodendrocytes has decayed by a maximum factor e relative to its maximum. As emphasized in [33], tracking the evolution of P_{size} provides insight into plaque formation dynamics. A decreasing P_{size} in time suggests that the demyelination process is intensifying, with destroyed oligodendrocytes concentrating in a specific region where d is strongly increasing. A sudden rise in the size of P_{size} signifies either the enlargement of a uniform lesion or the formation of secondary rings, depending on the value of χ. It is important to note that even before complete demyelination, where d is very small, P_{size} can still be of the order of centimeters. In fact, P_{size} represents the radius where myelin loss occurs, regardless of its severity (e.g., when dead oligodendrocytes $d\approx 1$). For a more specific measure of a highly demyelinated area, we introduce the quantity P'_{size}, which denotes the radius of the region where $d>d_{\mathrm{thresh}}$. Here, d_{thresh} is a threshold beyond which demyelination can be considered clinically significant. Here, we have set $d_{\mathrm{thresh}}=1/2$, *i.e.*, half of the maximum value of dead oligodendrocytes permitted. P'_{size} will stay at 0 until this threshold is met, after which it will progressively increase with plaque size. The third variable we consider is the maximum value M_P of the concentration of destroyed oligodendrocytes. This value, which ranges between 0 and 1 for our system, is significant because, at $M_P=1$, oligodendrocytes are completely destroyed. Therefore, it can be employed to predict the duration required to attain full demyelination. The final variable we will investigate is the time m_t necessary for M_P to reach a value of 1 (complete demyelination).

We first consider the case $\chi=4$ below the threshold χ_c for all the ξ values considered. The simulation outcomes reveal that increasing ξ causes a slowdown in the demyelination process. The results for $\xi=0.05,0.1,0.4,0.6$ are depicted in Figs. 8(a)–8(d), which display the profiles of destroyed oligodendrocytes at time $T=140$ days. Figs. 9(a)–9(d) illustrate the time evolution of quantities M_p, m_t, and P_{size}. From Figs. 8(a)–8(d), it is clear that a radially symmetric homogeneous plaque forms in all scenarios. The size and time of plaque formation are significantly affected by the value of ξ. Notably, when $\xi=0.01$, the plaque forms earlier and has a substantial spatial extent at the time shown. As ξ increases, the plaques become smaller, or in the case of $\xi=0.4,0.6$, not fully developed. This delay in the formation of plaque as the ξ values increase is further emphasized by the temporal progression of $M_P, m_t, P_{size}, P'_{size}$ exhibited in Figs. 9(a)–9(d). The peak value of M_P increases later as ξ increases, and the complete demyelination takes longer, almost linearly proportional to ξ. Despite the higher ξ values, the plaque can still attain significant size, as depicted in Figs. 9(c)–9(d), although this process takes longer. One can deduce from Fig. 9(c) that there is an intense demyelination phase characterized by a reduction in P_{size}, which indicates a quick concentration of damaged oligodendrocytes in a small region. This is followed by a sudden expansion that marks the growth of the demyelinated area. In Fig. 9(d), we observe that demyelination becomes significant approximately at the same time as $P'_{size}>0$, and subsequently increases as a further indication of the plaque size increase.

The second scenario pertains to the case $\chi=18$ above the critical threshold χ_c for all considered ξ values. This indicates that the condition to support Turing instability is satisfied, and the formation of concentric ring patterns is expected. For $\chi>\chi_c$, the case with the smallest ξ displays a more pronounced expansion of the plaque in comparison to the cases with higher ξ values, which is manifested by the development of multiple rings. The results are depicted in Figs. 10(a)–10(d), where the profiles of destroyed oligodendrocytes are shown for various ξ values at $T=120$ days. The concentric plaque has developed and extended only in the instances where $\xi=0.05,0.1$, whereas demyelination is only weak for $\xi=0.4,0.6$, at maximum d values of around 10^{-4}. However, plaques with concentric rings form later, as shown in Figs. 11(a)–11(b) at times $T=300,472$ days for $\xi=0.4,0.6$ respectively. In Figs. 12(a)–12(c) the time evolution of $M_p, m_t, P_{size}, P'_{size}$ is displayed. It can be concluded that similarly to the case $\chi=4$: (i) As ξ increases, full demyelination occurs over

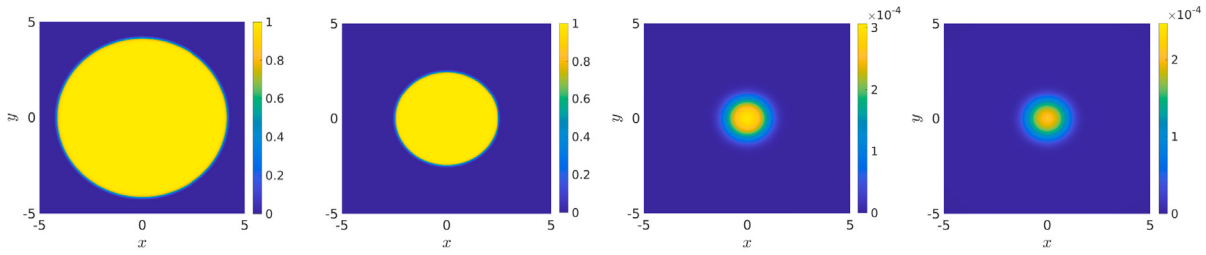

(a) $\xi = 0.05$ (b) $\xi = 0.1$ (c) $\xi = 0.4$ (d) $\xi = 0.6$

Fig. 8. Profile of destroyed oligodendrocytes d at time $T = 140$ days for $\chi = 4 < \chi_c$ and various ξ. The Initial condition is a bump for cytokine c, uniformly distributed small macrophages m concentrations over a small patch, and zero for the dead oligodendrocytes. Unit length is cm. For large ξ the plaque formation process is slowed down compared to the case of smaller ξ.

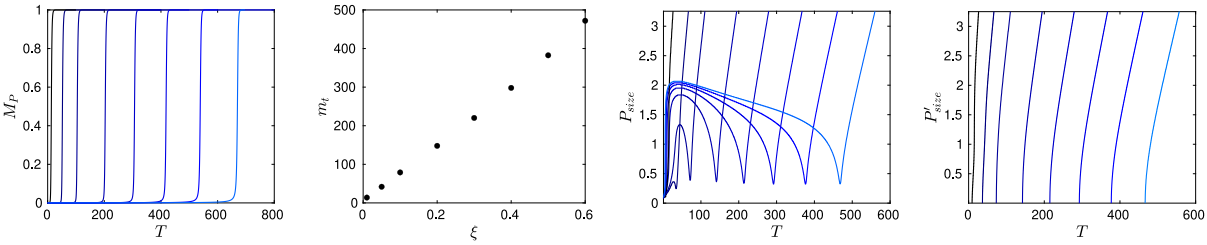

(a) (b) (c) (d)

Fig. 9. (a) Time evolution of the maximum value M_p of the destroyed oligodendrocytes distribution for $\xi = 0.01, 0.050.1, 0.2, 0.3, 0.4, 0.5, 0.6$ (left to right/black to light blue)(b) Times m_t at which $M_p = 1$ for the first time (full demyelination) for different values of ξ (c) Time evolution of P_{size} (in cm) for $\xi = 0.01, 0.050.1, 0.2, 0.3, 0.4, 0.5, 0.6$ (left to right/black to light blue) (d) Time evolution of P'_{size} (in cm) for $\xi = 0.01, 0.050.1, 0.2, 0.3, 0.4, 0.5, 0.6$ (left to right/black to light blue). All the figures are for $\chi = 4 < \chi_c$. Initial condition is a bump for cytokine c of magnitude 0.5, uniformly distributed small macrophages m concentrations of magnitude 10^{-3} over a small patch, and zero for the dead oligodendrocytes. Time unit is 1 day. (For interpretation of the references to color in this figure legend, the reader is referred to the web version of this article.)

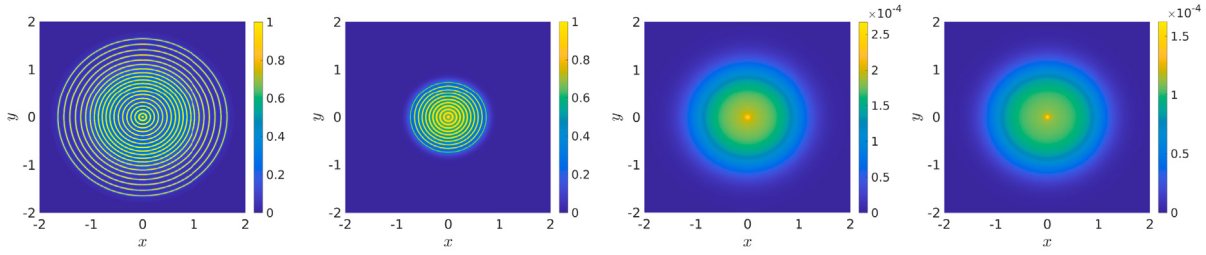

(a) $\xi = 0.05$ (b) $\xi = 0.1$ (c) $\xi = 0.4$ (d) $\xi = 0.6$

Fig. 10. Profile of destroyed oligodendrocytes at time $T = 120$ days for $\chi = 18 < \chi_c$ and various ξ. The Initial condition is a bump for cytokine c, uniformly distributed small macrophages m concentrations over a small patch, and zero for the dead oligodendrocytes. Unit length is cm. For $\xi = 0.05, 0.2$ concentric rings representing the typical Balo's sclerosis lesions are formed and largely extended. For $\xi = 0.4, 0.6$ lesions develop at later times (see Figs. 11(a)–11(b)).

a more prolonged period, resulting in the increase of both M_p and m_t, as illustrated in Figs. 12(a)–12(b); (ii) the onset of the intense demyelination phase is characterized by a reduction in P_{size} suddenly followed by a rapid growth and by the activation of P'_{size}, which happens earlier as ξ decreases. In contrast to the case with $\chi = 4$, the plaque subsequently expands, forming concentric rings. The jumps that appear in the sizes of P_{size} and P'_{size} indicate the formation of new rings.

6.2. Pre-active lesions

In this Subsection, we present the occurrence of pre-active lesions, which are clusters of activated microglia found in normal-appearing white matter without full demyelination. Pre-active lesions are considered the initial indicators of early reversible disorder and precede classical inflammatory lesions characterized by myelin degradation, following a well-accepted scenario of lesion development. Lesions can last for days to months and may resolve spontaneously, but they can also become chronic and exacerbate the disease. The majority of Multiple Sclerosis patients typically display the same pattern found in numerous

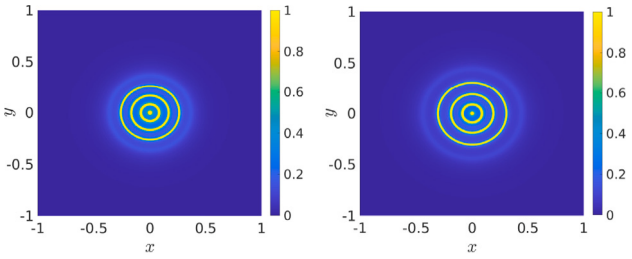

(a) $\xi = 0.4$ (b) $\xi = 0.6$

Fig. 11. Profile of destroyed oligodendrocytes d for $\chi = 18 > \chi_c$ for $\xi = 0.4, 0.6$. In all cases profiles are shown just after the formation of the third concentric ring. Initial condition is a bump for cytokine c of magnitude 0.5, a uniform concentration of small macrophages m with a magnitude of 10^{-3} over the region with excited cytokines, and zero dead oligodendrocytes. Times are $T = 300, 472$ days for $\xi = 0.4, 0.6$ respectively. Unit length is cm.

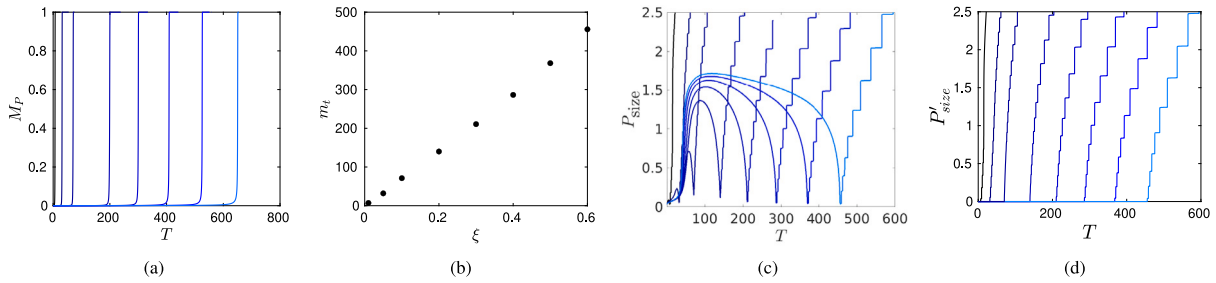

(a) (b) (c) (d)

Fig. 12. (a) Time evolution of the maximum value M_p of the destroyed oligodendrocytes distribution (b) Times m_t at which $M_p = 1$ for the first time (full demyelination) and times d_t at which M_p has its maximum in time, for different values of various ξ (c) Time evolution of P_{size} (in cm). (d) Time evolution of P'_{size} (in cm) for $\xi = 0.01, 0.050.1, 0.2, 0.3, 0.4, 0.5, 0.6$ (left to right/black to light blue) All the figures are for $\chi = 18 > \chi_c$. Initial condition is a bump for cytokine c of magnitude 0.5, a uniform concentration of small macrophages m with a magnitude of 10^{-3} over the region with excited cytokines, and zero dead oligodendrocytes. Time unit is 1 day. (For interpretation of the references to color in this figure legend, the reader is referred to the web version of this article.)

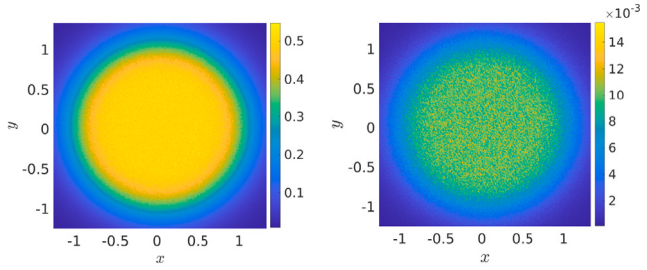

(a) $c, T = 0$ (b) $m, T = 0$

Fig. 13. Initial condition for the pre-active lesion simulation. A noised cytokine bumps over a rounded patch (panel a), noised distributed small macrophage concentrations m (panel b), and zero dead oligodendrocytes. Unit length is cm.

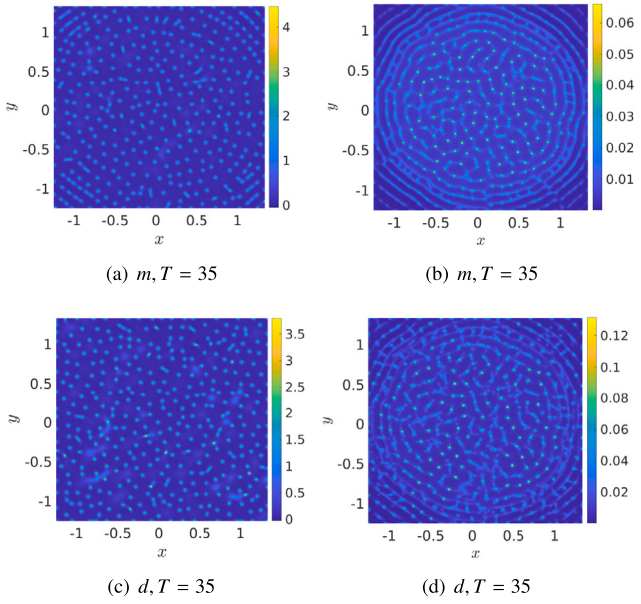

(a) $m, T = 35$ (b) $m, T = 35$

(c) $d, T = 35$ (d) $d, T = 35$

Fig. 14. Spatial distribution of activate macrophages m (panels a and c) and destroyed oligodendrocytes d (panels b and d) at times $T = 35$ days and $T = 70$ days, respectively, for $\chi = 10$, $\xi = 0.1$, $r = 0.001$, $\beta = 1$, $\delta = 0$, $\epsilon = 0.5$. Initial condition is depicted in Figs. 13(a)–13(b). Unit length is cm. Although there are many clusters of high-density activated macrophages ($m > 1$), demyelination is still moderate-weak ($d \lessapprox 0.1$)

experimental findings [69,70]. In [33], the model reproduced pre-active lesions within specific parameter ranges, namely for very low aggressiveness parameter r, usually of the order of 10^{-2}. They were observed a few days after development. Here, we want to show that cytokine-mediated macrophage production can slow down the development of these lesions, resulting in activated microglia clusters accompanied by mild demyelination that persists for several weeks. This scenario's initial condition comprises randomly distributed cytokine concentrations over a circular region (Fig. 13(a)). Small macrophage concentrations m are also randomly distributed over the same region (Fig. 13(b)), and no oligodendrocytes have been damaged ($d = 0$). The spatial distributions of m and d at different times are depicted in Figs. 14(a)–14(d) for the following parameters: $\chi = 10$, $\xi = 0.6$, $r = 0.001$, $\beta = 1$, $\delta = 0$, $\epsilon = 0.5$. Clusters of activated macrophages, with $m > 1$, and sparsely populated aggregates of damaged oligodendrocytes, with $d \lessapprox 0.15$, can be observed at 35–70 days.

6.3. Confluent plaques

This Section presents simulations on the coalescence of plaques that result in the formation of non-concentric lesions. The initial conditions for these simulations consist of three cytokine bumps with a magnitude of 0.5 and small macrophage concentrations (m) of magnitude 10^{-3}, uniformly distributed across an irregular patch bordering the cytokine bumps. Additionally, there are no dead oligodendrocytes. This configuration aims to model the progression of a single plaque originating from distinct multifocal damage zones, mimicking the frequently observed pattern in Magnetic Resonance Imaging scans of patients with Multiple Sclerosis. The parameters for the simulations are set as follows: $\beta = 1$, $\epsilon = 0.5$, $\delta = 1$, $r = 1$, $\tau = 1$, and $\xi = 0.2$. We investigate the above and below the critical χ_c cases, solving for the values $\chi = 4$ and $\chi = 18$. The lesions formed are depicted in Figs. 15(a)–15(b) and 16(a)–16(b). We present the profiles of destroyed oligodendrocytes d for the two scenarios $\xi = 4$ and $\xi = 18$. As expected, in the first scenario, a uniform plaque emerges once the damaged areas initially defined by the three cytokine bumps have conjoined. On the other hand, in the second scenario, an irregular pattern is observed, characterized by fragmented demyelinated rings. These lesions appear similar to those identified in MRI scans, as demonstrated in [71,72]. Without showing further simulations, we emphasize that for this setting also, the ξ parameter strongly influences the time of complete demyelination and subsequent lesion expansion. In fact, as explained in Section 6.1, the duration of these times can be altered by adjusting ξ, resulting in lesion growth ranging from a few days to several months.

7. Global well posedness

In this Section we shall study the well-posedness of the following system:

$$\begin{cases} \dfrac{\partial m}{\partial t} = \Delta m - \nabla \cdot (\chi(m)\nabla c) + c\, m(1-m)\,, & (t,x) \in \Omega_T \\ \dfrac{\partial c}{\partial t} = \dfrac{1}{\tau}\left(\epsilon \Delta c + \delta d - c + \beta m\right), & (t,x) \in \Omega_T \\ \dfrac{\partial d}{\partial t} = rF(m)\, m\,(1-d)\,, & (t,x) \in \Omega_T \end{cases} \tag{7.1}$$

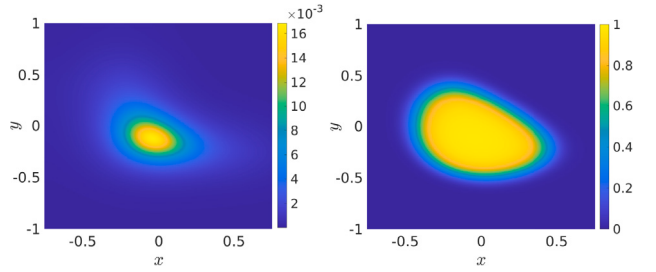

(a) $d, T = 200$ (b) $d, T = 260$

Fig. 15. Profile of destroyed oligodendrocytes d at times $T = 200$ and $T = 260$ days for parameters $\chi = 4 < \chi_c$. The Initial condition is made by three cytokine bumps, uniformly distributed small macrophage concentrations m, and zero dead oligodendrocytes. Unit length is cm. A uniform large plaques forms after the confluence of the damaged areas initially defined by the three cytokine bumps.

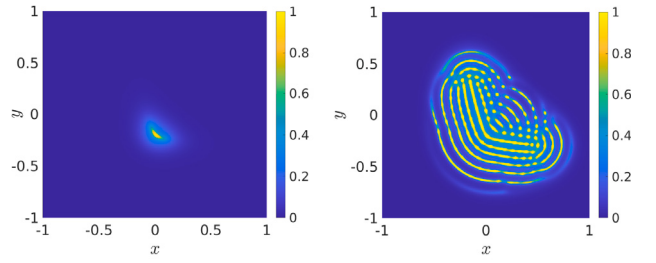

(a) $d, T = 200$ (b) $d, T = 260$

Fig. 16. Profile of destroyed oligodendrocytes d at times $T = 200$ and $T = 260$ days for parameters $\chi = 18 > \chi_c$. The Initial condition is made by three cytokine bumps, uniformly distributed small macrophage concentrations m, and zero dead oligodendrocytes. Unit length is cm. A patterned large plaques forms after the confluence of the damaged areas initially defined by the three cytokine bumps.

with $\chi(m) = \chi \frac{m}{1+m}$, $F(m) = \frac{m}{1+m}$, $\Omega_T = (0,T)\times\Omega$, where Ω is a bounded domain in $\mathbb{R}^n$ ($n \in \mathbb{N}$, $n \geq 1$) with smooth boundary $\partial\Omega$. We denote by $\mathbf{n} = \mathbf{n}(s)$ the outward normal to $\partial\Omega$ at a point s of the boundary, and impose the following Neumann boundary condition on $\partial\Omega$:

$$\begin{cases} \mathbf{n}\cdot\nabla m = 0\,, \\ \mathbf{n}\cdot\nabla c = 0\,. \end{cases} \tag{7.2}$$

Finally, we impose the following non-negative initial conditions:

$$\begin{cases} m(t=0,x) = m_{in}(x)\,, & x \in \Omega \\ c(t=0,x) = c_{in}(x)\,, & x \in \Omega \\ d(t=0,x) = d_{in}(x)\,. & x \in \Omega \end{cases} \tag{7.3}$$

Moreover, we recall the following conditions on the system parameters:

$$\chi > 0\,, \quad \tau > 0\,, \quad \epsilon > 0\,, \quad \beta \geq 0\,, \quad r > 0\,, \quad \delta \geq 0\,. \tag{7.4}$$

The system (7.1) differs from the system (2.3) in the kinetic term of the macrophage equation. In the first equation of (7.1), differently from (2.3), the production mechanism of the activated macrophages has no saturation effect. This means that the term $c/(\xi + c)$ of the first equation of (2.3), is substituted by c in (7.1). The functional form of (7.1) corresponds to the limit of infinite saturation constant k, and derives from (2.1) as follows: first, rescale as $\lambda \to k\lambda$, $\tilde{k}_c \to k\,\tilde{k}_c$; second, take the limit $k \to \infty$; finally, adimensionalize as in (2.2).

Clearly, for the analysis of the existence and uniqueness of the solution, the system (7.1) is more challenging than the system (2.3). Regularity results for system (2.3) could be immediately recovered from the results obtained in [52–54]. On the other hand, the fact that the system (7.1) presents a linear growth in c for the macrophage production term requires some modifications of the arguments in [52–54]. In the rest of this Section, we shall follow [54].

We begin by introducing some classical mathematical notations, see [73,74]. We shall use the $L^p(\Omega)$ function spaces with $p \geq 1$ and denote by $\|\cdot\|_{L^p(\Omega)}$ the norm. For the space $L^\infty(\Omega)$, we shall use the ess-sup norm, denoted by $\|\cdot\|_{L^\infty(\Omega)}$.

For any t_0, with $0 \leq t_0 < T$, we denote by $\Omega_{t_0,T} := (t_0,T)\times\Omega$. For simplicity, when $t_0 = 0$, we denote by Ω_T the set $\Omega_{0,T}$. The spaces $L^p(\Omega_{t_0,T})$, with $1 \leq p \leq \infty$, are the spaces $L^p((t_0,T), L^p(\Omega))$ equipped with the classical space–time norm which is denoted by $\|\cdot\|_{L^p(\Omega_{t_0,T})}$.

When $t_0 = 0$, we write $L^p(\Omega_T)$ and $L^\infty(\Omega_T)$, and the norms are denoted by $\|\cdot\|_{L^p(\Omega_T)}$ and $\|\cdot\|_{L^\infty(\Omega_T)}$.

As usual, $W^{r,p}(\Omega)$ are the Sobolev spaces of L^p functions with differential index r, where $1 \leq p \leq \infty$ and $r > 0$.

We shall consider also the space $W_p^{1,2}(\Omega_{t_0,T})$ defined as:

$$W_p^{1,2}(\Omega_{t_0,T}) = \Big\{ v : \partial_t^r \partial_x^s v \in L^p(\Omega_{t_0,T}), \quad 2r + s \leq 2,\ r,s \in \mathbb{N}\cup\{0\} \Big\},$$

with norm:

$$\|v\|_{W_p^{1,2}(\Omega_{t_0,T})} := \sum_{2r+s\leq 2} \|\partial_t^r \partial_x^s v\|_{L^p(\Omega_{t_0,T})}.$$

By $C^k(\overline{\Omega})$ we denote the Banach space of continuous functions in $\overline{\Omega}$, such that their derivatives up to order k are continuous in $\overline{\Omega}$.

The space $C^0\left(\Omega_T\right)$ is the space of continuous function in Ω_T.

Finally, we introduce the function space $C^{0,1} := C^{0,1}\left([0,T]\times\overline{\Omega}\right)$, that is the space of functions continuous, together with their space gradient, in $[0,T]\times\overline{\Omega}$. The space $C^{0,1}$ is a Banach space with norm:

$$\|u\|_{C^{0,1}} = \sup_{t\in[0,T]} \|u(t,\cdot)\|_{L^\infty(\Omega)} + \sup_{t\in[0,T]} \|\nabla u(t,\cdot)\|_{L^\infty(\Omega)}.$$

The main result of this Section is the following Theorem:

Theorem 7.1. *Let Ω be a smooth ($C^{2+\alpha}$, with $\alpha > 0$) bounded connected open subset of $\mathbb{R}^n$, $n \in \mathbb{N}$, and suppose that (7.4) holds. For $\tilde{p} > n+2$, let the non-negative initial conditions m_{in} and c_{in} belong to $W^{(2-2/\tilde{p}),\tilde{p}}(\Omega)$, while d_{in} belongs to $L^\infty(\Omega)$. Then the system (7.1) with boundary and initial conditions (7.2) and (7.3) admits a unique global strong solution which is non-negative in each component and bounded in time. More precisely, we have that:*

$$\partial_t m\,,\ \partial_t c\,,\ \partial_t d\,,\ \Delta m\,,\ \Delta c\,,\ \nabla\cdot(\chi(m)\nabla c) \quad \in L^{\tilde{p}}\left(\Omega_T\right)\,, \tag{7.5}$$

and

$$m\,,\ c \in C^{0,1}\,, \quad d \in L^\infty(\Omega_T)\,, \tag{7.6}$$

for all $T > 0$.

Finally, if the initial data are smooth, i.e., m_{in}, c_{in} and $d_{in} \in C^2(\overline{\Omega})$ and satisfy the compatibility conditions $\nabla m_{in}\cdot\mathbf{n} = \nabla c_{in}\cdot\mathbf{n} = 0$ on $\partial\Omega$, then the solution to system (7.1) is classical, i.e.,

$$\partial_t m\,,\ \partial_t c\,,\ \partial_t d\,,\ \Delta m\,,\ \Delta c\,,\ \nabla\cdot(\chi(m)\nabla c) \in C^0\left(\Omega_T\right)\ \forall T > 0\,. \tag{7.7}$$

The proof of Theorem 7.1 is divided into two parts: in Section 7.1, we shall prove the existence of a global solution; in Section 7.2, we shall prove the uniqueness. The proof of Theorem 7.1 closely follows the procedure adopted in [54].

We recall the following embedding Lemma, see [54,74,75], which will be useful in the sequel.

Lemma 7.2. *Assume that $1 < p < \infty$ and fix $T > 0$ and $t_0 \in [0,T)$. Then there exists a constant C which depends on $T - t_0$, Ω, p and n, such that for all $u \in W_p^{1,2}(\Omega_{t_0,T})$ we have:*

- $$\|u\|_{L^q(\Omega_{t_0,T})} \leq C\|u\|_{W_p^{1,2}(\Omega_{t_0,T})}\,,$$

$$\text{where} \quad \begin{cases} q = \frac{(n+2)p}{n+2-2p} & \text{if } p < \frac{n+2}{2}\,; \\ q = \infty & \text{if } p > \frac{n+2}{2}\,; \\ q \text{ is finite and arbitrary} & \text{if } p = \frac{n+2}{2}\,. \end{cases} \tag{7.8}$$

- $$\|\nabla u\|_{L^q(\Omega_{t_0,T})} \le C \|u\|_{W_p^{1,2}(\Omega_{t_0,T})}\,,$$

$$\text{where} \quad \begin{cases} q = \frac{(n+2)p}{n+2-p} & \text{if } p < n+2\,; \\ q = \infty & \text{if } p > n+2\,; \\ q \text{ is finite and arbitrary} & \text{if } p = n+2\,. \end{cases} \tag{7.9}$$

- $W_p^{1,2}(\Omega_{t_0,T})$ *is compactly embedded in* $C^{0,1}$, *if* $p > n+2$.

7.1. Global existence

In this Subsection, first, using the Leray–Schauder fixed point theorem [73], we shall prove the existence of global non negative solutions to system (7.1). Second, we shall prove that such solutions are bounded in the L^∞-norm.

7.1.1. Construction of the map S

We construct the map S

$$S : C^{0,1} \times C^{0,1} \times [0,1] \longrightarrow C^{0,1} \times C^{0,1}\,, \tag{7.10}$$

as follows:

- for a given $m \in C^{0,1}$, solve the following ODE:

$$\begin{cases} \frac{\partial d}{\partial t} = r\, F(m_+)\, m_+\, (1-d) & (t,x) \in \Omega_T\,, \\ d(t=0,x) = d_{in}(x) & x \in \Omega\,, \end{cases} \tag{7.11}$$

  where $m_+ = \max(0, m)$;
- next, solve the following heat equation with source term and Neumann boundary condition:

$$\begin{cases} \frac{\partial c^*}{\partial t} = \frac{1}{\tau}\left[\epsilon \Delta c^* - c^* + \left(\delta d + \beta m_+\right)\right] & (t,x) \in \Omega_T\,, \\ \mathbf{n} \cdot \boldsymbol{\nabla} c^* = 0 & (t,s) \in (0,T) \times \partial\Omega\,, \\ c^*(t=0,x) = c_{in}(x) & x \in \Omega\,; \end{cases} \tag{7.12}$$

- finally, solve the following heat equation with source term and Neumann boundary condition:

$$\begin{cases} \frac{\partial m^*}{\partial t} = \Delta m^* + m_+(1-m_+)c^* - \nabla \cdot \left(\chi(m_+)\nabla c^*\right) & (t,x) \in \Omega_T\,, \\ \mathbf{n} \cdot \boldsymbol{\nabla} m^* = 0 & (t,s) \in (0,T) \times \partial\Omega\,, \\ m^*(x,0) = m_{in}(x) & x \in \Omega\,, \end{cases} \tag{7.13}$$

The map S is defined as

$$S(m, c, \lambda) = (\lambda\, m^*, \lambda\, c^*). \tag{7.14}$$

Remark 7.3. From (7.11) and $d_{in} \ge 0$, immediately follows that

$$0 \le d(t,x) \le \max(1, \|d_{in}\|_{L^\infty(\Omega)}) = H_0\,. \tag{7.15}$$

To apply the Leray–Schauder theorem, we define the following set $\boldsymbol{\Phi}$:

$$\boldsymbol{\Phi} = \left\{(m,c) \in C^{0,1} \times C^{0,1} \,:\, S(m,c,\lambda) = (m,c),\ 0 < \lambda \le 1\right\}. \tag{7.16}$$

Observe that if $(m,c) \in \boldsymbol{\Phi}$, then $m = \lambda m^*$ and $c = \lambda c^*$ where m^* and c^* solve (7.12) and (7.13).

Lemma 7.4. *If* (m,c) *are in* $\boldsymbol{\Phi}$, *then* m *and* c *are non negative.*

Proof. We first observe that if $(m,c) \in \boldsymbol{\Phi}$, then m and c satisfy the following two systems of equations:

$$\begin{cases} \frac{\partial c}{\partial t} = \frac{1}{\tau}\left[\epsilon \Delta c - c + \lambda\left(\delta d + \beta m_+\right)\right] & (t,x) \in \Omega_T\,, \\ \mathbf{n} \cdot \boldsymbol{\nabla} c = 0 & (t,s) \in (0,T) \times \partial\Omega\,, \\ c(t=0,x) = \lambda\, c_{in}(x) & x \in \Omega\,; \end{cases} \tag{7.17a}$$

$$\begin{cases} \frac{\partial m}{\partial t} = \Delta m + m_+(1-m_+)c - \nabla \cdot \left(\chi(m_+)\nabla c\right) & (t,x) \in \Omega_T\,, \\ \mathbf{n} \cdot \boldsymbol{\nabla} m = 0 & (t,s) \in (0,T) \times \partial\Omega\,, \\ m(t=0,x) = \lambda\, m_{in}(x) & x \in \Omega\,. \end{cases} \tag{7.17b}$$

Eq. (7.17a) and $c_{in} \ge 0$ and $d \ge 0$, imply that $c \ge 0$.

To prove that $m \ge 0$, we multiply the first equation in (7.17b) by m_-^2, where $m_- = \max(0, -m)$, and integrate in space and time. After integration by parts, we obtain:

$$\begin{aligned} &-\frac{1}{3}\int_\Omega m_-^3\, dx = 2\int_0^t \int_\Omega m_- |\nabla m_-|^2 dx dt \\ &+ \int_0^t \int_\Omega m_-^2\, m_+(1-m_+) c\, dx dt - 2\chi \int_0^t \int_\Omega \frac{m_- m_+}{1+m_+} \nabla m_- \cdot \nabla c\, dx dt \\ &= 2\int_0^t \int_\Omega m_- |\nabla m_-|^2 dx dt \ge 0\,, \end{aligned}$$

and consequently $m_- = 0$ for each $t \in [0,T]$, which concludes the proof. □

As a consequence of Lemma 7.4 and of the definition of $\boldsymbol{\Phi}$, we have that, if $(m,c) \in \boldsymbol{\Phi}$, then (m,c,d) satisfies the following system for $(t,x) \in \Omega_T$:

$$\begin{cases} \frac{\partial m}{\partial t} = \Delta m + m(1-m)\, c - \nabla \cdot (\chi(m)\nabla c)\,, \\ \frac{\partial c}{\partial t} = \frac{1}{\tau}\left[\epsilon \Delta c - c + \lambda\left(\delta d + \beta m\right)\right]\,, \\ \frac{\partial d}{\partial t} = r F(m) m\,(1-d)\,, \end{cases} \tag{7.18a}$$

with Neumann BC and the following initial condition for $x \in \Omega$:

$$\begin{cases} m(x, t=0) = \lambda m_{in}(x)\,, \\ c(x, t=0) = \lambda c_{in}(x)\,, \\ d(x, t=0) = d_{in}(x)\,. \end{cases} \tag{7.18b}$$

7.1.2. Compactness and continuity of S

To apply the Leray–Schauder fixed point theorem, we need to prove that the map S is compact and continuous in $C^{0,1} \times C^{0,1}$.

We shall divide the proof in two Lemmas: in Lemma 7.5 we shall prove that S sends bounded sets of $C^{0,1} \times C^{0,1} \times [0,1]$ into precompact sets of $C^{0,1} \times C^{0,1}$; then, in Lemma 7.6, we shall prove that S is continuous.

Lemma 7.5. *Under the hypotheses of Theorem 7.1, the map* S *maps bounded sets of* $C^{0,1} \times C^{0,1} \times [0,1]$ *into precompact sets of* $C^{0,1} \times C^{0,1}$.

Proof. From the definition of the map S given by (7.10)–(7.13), from the maximal regularity results of the heat equation with Neumann boundary conditions [54,74], and from (7.15), we have that:

$$\|c^*\|_{W_p^{1,2}(\Omega \times (0,T))} \le C_p\,,$$
$$\|m^*\|_{W_p^{1,2}(\Omega \times (0,T))} \le C_p\,,$$

where the constant C_p depends on $\|m\|_{C^{0,1}}$, Ω, T, $\|m_{in}\|_{L^\infty(\Omega)}$, $\|c_{in}\|_{L^\infty(\Omega)}$, and $\|d_{in}\|_{L^\infty(\Omega)}$. Since $p > n+2$, then $W_p^{2,1}(\Omega_T)$ is compactly embedded in $C^{0,1}$ and the Lemma is proved. □

Lemma 7.6. *Under the hypotheses of Theorem 7.1. the map* S *is continuous.*

Proof. Consider $m_1, m_2 \in C^{0,1}$ and $c_1, c_2 \in C^{0,1}$. Denote by d_1 and d_2 the solutions of (7.11) obtained for m_1 and m_2, respectively. We have:

$$\|d_1 - d_2\|_{L^\infty(\Omega_T)} \le C_T \|m_{1+} - m_{2+}\|_{L^\infty(\Omega_T)} \le C_T \|m_1 - m_2\|_{C^{0,1}}\,, \tag{7.19}$$

where C_T is a constant which depends on T, r and $\|d_{in}\|_{L^\infty(\Omega)}$. Moreover, considering the equation satisfied by $c_1^* - c_2^*$, using the maximal regularity results together with (7.19), and the compactly embedding property of $W_p^{1,2}$ for $p > n+2$, we obtain that:

$$\|c_1^* - c_2^*\|_{C^{0,1}} \le C_T \|m_1 - m_2\|_{C^{0,1}}\,, \tag{7.20}$$

where again we denote by C_T a constant which depends on T, β, δ, ϵ, τ, r, Ω, n and $\|d_{in}\|_{L^\infty(\Omega)}$. We now consider the following equation for $m_1^* - m_2^*$:

$$\frac{\partial(m_1^* - m_2^*)}{\partial t} = \Delta(m_1^* - m_2^*) + m_{1+}(1-m_{1+})c_1^* - m_{2+}(1-m_{2+})c_2^* +$$
$$-\nabla\cdot\left(\chi(m_{1+})\nabla c_1^* - \chi(m_{1+})\nabla c_1^*\right) \quad \text{with } (t,x) \in \Omega_T\,,$$

with boundary condition:

$$\nabla(m_1^* - m_1^*)\cdot \mathbf{n} = 0\,, \qquad (s,t) \in (0,T)\times\partial\Omega,$$

and initial condition:

$$m_1^*(x,0) - m_2^*(x,0) = 0\,, \qquad x \in \Omega.$$

We have the following estimates:

$$|m_{1+}(1-m_{1+})c_1^* - m_{2+}(1-m_{2+})c_2^*| \le$$
$$\le |m_{1+}(1-m_{1+})(c_1^* - c_2^*)| + |(m_{1+}(1-m_{1+}) - m_{2+}(1-m_{2+}))c_2^*|$$
$$\le \frac{1}{4}|c_1^* - c_2^*| + |m_1 - m_2||c_2^*|(1 + 2\max(m_{1+}, m_{2+}))\,,$$

and

$$|\nabla\cdot\left(\chi(m_{1+})\nabla c_1^* - \chi(m_{2+})\nabla c_2^*\right)| \le$$
$$\le |\chi(m_{1+})|\,|\Delta(c_1^* - c_2^*)| + |\nabla\chi(m_{1+})|\,|\nabla c_1^* - \nabla c_2^*| +$$
$$+|\chi(m_{1+}) - \chi(m_{2+})|\,|\Delta c_2^*| + |\nabla(\chi(m_{1+}) - \chi(m_{1+}))|\,|\nabla c_2^*|$$
$$\le \chi\,|\Delta(c_1^* - c_2^*)| + \chi\,|\nabla m_{1+}|\,|\nabla c_1^* - \nabla c_2^*| +$$
$$+\chi|m_{1+} - m_{2+}|\,|\Delta c_2^*| + \chi|\nabla(m_{1+} - m_{2+})|\,|\nabla c_2^*|\,.$$

Repeating the same arguments used for $c_1^* - c_2^*$, we have:

$$\|m_1^* - m_2^*\|_{C^{0,1}} \le C_T \|m_1 - m_2\|_{C^{0,1}}\,, \tag{7.21}$$

where C_T is a constant which depends on T, β, δ, ϵ, τ, r, Ω, n, χ and $\|d_{in}\|_{L^\infty(\Omega)}$. From (7.20) and (7.21), we have that the map S is continuous from $C^{0,1}\times C^{0,1}\times[0,1]$ to $C^{0,1}\times C^{0,1}$. □

7.1.3. Boundedness of Φ

We want to prove that Φ is bounded in $C^{0,1}\times C^{0,1}$. The proof of this is given in Lemma 7.11. Before stating the lemma and giving the proof, we need four lemmas on regularity of m and c, when (m,c) is in Φ.

Lemma 7.7. *Let $(m,c) \in \Phi$. Under the hypotheses of Theorem 7.1, there exists a constant H_1 that depends on T, Ω, n, β, δ, τ, $\|m_{in}\|_{L^1(\Omega)}$, $\|c_{in}\|_{L^1(\Omega)}$, $\|d_{in}\|_{L^\infty(\Omega)}$ but not on λ, such that*

$$\sup_{t\in[0,T]}\left(\|m(t,\cdot)\|_{L^1(\Omega)} + \|c(t,\cdot)\|_{L^1(\Omega)}\right) \le H_1\,. \tag{7.22}$$

Proof. Integrating the equations for m and c in (7.18a) and summing, we obtain:

$$\frac{d}{dt}\int_\Omega (m+c)\,dx \le \int_\Omega (m-m^2)c\,dx - \frac{1}{\tau}\int_\Omega c\,dx + \frac{\beta}{\tau}\int_\Omega m\,dx$$
$$+\frac{\delta}{\tau}|\Omega|\,\|d\|_{L^\infty(\Omega)}$$
$$\le \left(\frac{1}{4} - \frac{1}{\tau}\right)\int_\Omega c\,dx + \frac{\beta}{\tau}\int_\Omega m\,dx + \frac{\delta}{\tau}|\Omega|\,\|d\|_{L^\infty(\Omega)}$$
$$\le \max\left(\frac{\beta}{\tau}, \frac{1}{4} - \frac{1}{\tau}\right)\int_\Omega (m+c)\,dx + \frac{\delta}{\tau}|\Omega|H_0\,,$$

where we have used the inequality $m(1-m) \le 1/4$ and we have denoted by $|\Omega|$ the measure of the domain Ω. Consequently, by using Gronwall's lemma [76], we obtain (7.22) with

$$H_1 = \left(\|m_{in}\|_{L^1(\Omega)} + \|c_{in}\|_{L^1(\Omega)} + \frac{\delta}{\tau}|\Omega|TH_0\right)e^{\left(\max\left(\frac{\beta}{\tau}, \frac{1}{4}-\frac{1}{\tau}\right)T\right)}.$$ □

Lemma 7.8. *Let $(m,c) \in \Phi$. Under the hypotheses of Theorem 7.1, there exists a constant H_2 that depends on T, Ω, n, β, δ, τ, ϵ, $\|m_{in}\|_{L^2(\Omega)}$, $\|c_{in}\|_{L^2(\Omega)}$, $\|d_{in}\|_{L^\infty(\Omega)}$ but not on λ, such that:*

$$\|m\|_{L^2(\Omega_T)} \le H_2\,. \tag{7.23}$$

Proof. Consider the equation for m in (7.18a) and integrate in space:

$$\frac{d}{dt}\int_\Omega m dx = \int_\Omega (m - m^2)c\,dx$$
$$\le \int_\Omega (1-m)c\,dx = \|c\|_{L^1(\Omega)} - \|mc\|_{L^1(\Omega)}\,.$$

From the above bound and using (7.22), it follows that:

$$\|m\,c\|_{L^1(\Omega_T)} \le C^*\,, \tag{7.24}$$

where C^* is a constant which depends on T, Ω, n, β, δ, τ and $\|m_{in}\|_{L^1(\Omega)}$, $\|c_{in}\|_{L^1(\Omega)}$ and $\|d_{in}\|_{L^\infty(\Omega)}$, but not on λ. Consider now the equation for c in (7.18a), multiply times c and integrate in space to obtain:

$$\frac{1}{2}\frac{d}{dt}\int_\Omega c^2 dx + \frac{\epsilon}{\tau}\int_\Omega |\nabla c|^2 dx + \int_\Omega c^2 dx$$
$$\le \frac{\delta}{\tau}H_0\|c\|_{L^1(\Omega)} + \frac{\beta}{\tau}\|m\,c\|_{L^1(\Omega)}\,.$$

Consequently, using (7.22) and (7.24), there exists a constant C^{**} such that:

$$\sup_{t\in[0,T]}\|c\|_{L^2(\Omega)} + \|\nabla c\|^2_{L^2(\Omega_T)} \le C^{**}\,, \tag{7.25}$$

where C^{**} depends on T, Ω, n, β, δ, ϵ, τ and $\|m_{in}\|_{L^1(\Omega)}$, $\|c_{in}\|_{L^1(\Omega)}$ and $\|d_{in}\|_{L^\infty(\Omega)}$ but not on λ. We now multiply times m the equation for m in (7.18a) and integrate in space to obtain:

$$\frac{1}{2}\frac{d}{dt}\|m\|^2_{L^2(\Omega)} \le -\|\nabla m\|^2_{L^2(\Omega)} + \|m^2(1-m)\,c\|_{L^1(\Omega)}$$
$$+\|\chi(m)\,\nabla c\cdot\nabla m\|_{L^1(\Omega)}$$
$$\le -\|\nabla m\|^2_{L^2(\Omega)} + \frac{1}{4}\|m\,c\|_{L^1(\Omega)}$$
$$+\frac{1}{2}\|\chi(m)\,\nabla c\|^2_{L^2(\Omega)} + \frac{1}{2}\|\nabla m\|^2_{L^2(\Omega)}$$
$$\le -\frac{1}{2}\|\nabla m\|^2_{L^2(\Omega)} + \frac{1}{4}\|m\,c\|_{L^1(\Omega)} + \frac{1}{2}\chi^2\|\nabla c\|^2_{L^2(\Omega)}\,.$$

In the above estimate, using (7.24) and (7.25) and applying Gronwall's lemma we obtain (7.23). □

Lemma 7.9. *Let $(m,c) \in \Phi$. Under the hypotheses of Theorem 7.1, there exists a constant H_3 that depends on Ω, T, n, ϵ, τ, β, δ, $\|m_{in}\|_{L^2(\Omega)}$, $\|c_{in}\|_{W^{1,2}(\Omega)}$, $\|d_{in}\|_{L^\infty(\Omega)}$ but not on λ, such that:*

$$\|c\|_{W_2^{2,1}(\Omega_T)} \le H_3\,. \tag{7.26}$$

$$\|\nabla c\|_{L^{2+4/n}(\Omega_T)} \le C\,H_3\,. \tag{7.27}$$

Proof. To obtain (7.26), consider the equation for c in (7.18a) and use the maximal regularity result together with (7.15) and (7.23). Estimate (7.27) is a consequence of (7.26) and the embedding Lemma 7.2 (see Lemma 2.3 in [54]). □

Lemma 7.10.

Let $(m,c) \in \Phi$. Under the hypotheses of Theorem 7.1 and for $1 \le p < \infty$, there exists a constant H_p^* that depends on p, Ω, T, n, ϵ, τ, β, δ, $\|m_{in}\|_{W^{2-2/\bar{p},\bar{p}}(\Omega)}$, $\|c_{in}\|_{W^{2-2/\bar{p},\bar{p}}(\Omega)}$, and $\|d_{in}\|_{L^\infty(\Omega)}$, but not on λ, such that

$$\|m\|_{L^p(\Omega_T)} + \|c\|_{L^p(\Omega_T)} \le H_p^* . \tag{7.28}$$

Proof. For the proof we adapt to our case the proof of Lemma 2.4 in [54]. We prove (7.28) for p large enough, in particular for $p = p'/(p'-1)$, where p' is such that $1 < p' < \frac{n+2}{2}$. Consequently, we have that $1 + \frac{2}{n} < p < \infty$.

Let be $\theta \in L^{p'}(\Omega_T)$, with $\theta \ge 0$ and $\|\theta\|_{L^{p'}(\Omega_T)} \le 1$. We denote with ϕ and ψ the unique solutions of the following forward heat equations:

$$\begin{cases} \frac{\partial}{\partial t}\phi + \Delta\phi = -\theta & (t,x) \in \Omega_T , \\ \nabla\phi \cdot \mathbf{n} = 0 & (t,s) \in (0,T)\times\partial\Omega , \\ \phi(T,x) = 0 & x \in \Omega , \end{cases} \tag{7.29}$$

$$\begin{cases} \frac{\partial}{\partial t}\psi + \frac{\epsilon}{\tau}\Delta\psi = -\theta & (t,x) \in \Omega_T , \\ \nabla\psi \cdot \mathbf{n} = 0 & (t,s) \in (0,T)\times\partial\Omega , \\ \psi(T,x) = 0 & x \in \Omega . \end{cases} \tag{7.30}$$

We have that ϕ and ψ are nonnegative and, from the maximal regularity for the heat semigroup [54,74] and Lemma 7.2, we also have that:

$$\|\partial_t\phi\|_{L^{p'}(\Omega_T)} + \|\phi\|_{L^{q_1}(\Omega_T)} + \|\nabla\phi\|_{L^{q_2}(\Omega_T)} \le C_{p'} , \tag{7.31}$$

and

$$\|\partial_t\psi\|_{L^{p'}(\Omega_T)} + \|\psi\|_{L^{q_1}(\Omega_T)} + \|\nabla\psi\|_{L^{q_2}(\Omega_T)} \le C_{p'} , \tag{7.32}$$

where $q_1 = (n+2)p'/(n+2-2p')$ and $q_2 = (n+2)p'/(n+2-p')$ and $C_{p'}$ is a positive constant which depends on Ω, T, n and p'.

Multiply θ by m and integrate in space and time. Using Eq. (7.29), integrating by parts and using (7.18a), we obtain:

$$\int_0^T\int_\Omega m\theta\,dx\,dt \le \int_\Omega m_{in}\,\phi(0,x)\,dx + \frac{1}{4}\int_0^T\int_\Omega c\,\phi dx\,dt + \int_0^T\int_\Omega \chi(m)\nabla\phi\cdot\nabla c\,dx\,dt . \tag{7.33}$$

Analogously, multiply θ by c and integrate in space and time. Using Eq. (7.30), integrating by parts and using (7.18a), we obtain:

$$\int_0^T\int_\Omega c\theta\,dx\,dt \le \int_\Omega c_{in}\,\psi(0,x)\,dx + \frac{\delta}{\tau}\int_0^T\int_\Omega \psi\,d\,dx\,dt + \frac{\beta}{\tau}\int_0^T\int_\Omega m\psi dx\,dt . \tag{7.34}$$

We estimate each terms in the above inequalities.

We begin with the first term in (7.33). Using Holdër inequalities and (7.31), we have (see [54]):

$$\int_\Omega m_{in}\phi(0,x)dx \le \|m_{in}\|_{L^p(\Omega)}\|\phi(0,x)\|_{L^{p'}(\Omega)} \le \|m_{in}\|_{L^p(\Omega)}\,T^{1/p}\left\|\frac{\partial}{\partial_t}\phi\right\|_{L^{p'}(\Omega_T)} \le \|m_{in}\|_{L^p(\Omega)}\,T^{1/p}\,C_{p'} . \tag{7.35}$$

Repeating the same arguments for the first term in (7.34), we have

$$\int_\Omega c_{in}\psi(0,x)dx \le \|c_{in}\|_{L^p(\Omega)}\,T^{1/p}\,C_{p'} . \tag{7.36}$$

For the second term in (7.34), using (7.15) and (7.31), we have

$$\int_0^T\int_\Omega \psi\,d\,dx\,dt \le H_0\|\psi\|_{L^1(\Omega_T)} \le H_0C^*\|\psi\|_{L^{q_1}(\Omega_T)} \le H_0C^*C_{p'} . \tag{7.37}$$

In the rest of this proof, with C^* we shall denote a constant that depends on p, Ω, T and n.

We estimate now the second term in (7.33).

As in [54], we consider first the case when $n = 1,2$. In this case $q_1 > 2$ and using (7.26), (7.31) and Lemma 7.2, we obtain:

$$\int_0^T\int_\Omega c\phi\,dx\,dt \le \|c\|_{L^2(\Omega_T)}\|\phi\|_{L^2(\Omega_T)} \le C^*\,H_3\,C_{p'} . \tag{7.38}$$

When $n \ge 3$, repeating the same arguments in [54], we define $\sigma = 1 - 4/(n+2)$, which implies that $0 < \sigma < 1$. Using Holdër inequalities and using (7.26), (7.31) and Lemma 7.2, we have:

$$\int_0^T\int_\Omega c\,\phi\,dx\,dt \le C^*C_{p'}\,H_3^{1-\sigma}\,\|c\|^\sigma_{L^p(\Omega_T)} . \tag{7.39}$$

Analogously we have that

$$\int_0^T\int_\Omega m\,\psi\,dx\,dt \le C^*\,H_2\,C_{p'} + C^*C_{p'}\,H_2^{1-\sigma}\,\|m\|^\sigma_{L^p(\Omega_T)} . \tag{7.40}$$

Finally, we estimate the last term in (7.33). We choose $b \in (0,1]$ that satisfies the following condition:

$$0 < b < \frac{4}{n+2} . \tag{7.41}$$

Notice that one has

$$\chi(m) = \chi\frac{m}{1+m} \le \chi m^b . \tag{7.42}$$

From (7.41), there exists an s, with $s \in (0,1)$, such that

$$b - s < \frac{2}{n+2} , \quad b - s < \frac{4}{n+2} - 1 . \tag{7.43}$$

Using (7.42), Holdër inequalities and using (7.23), (7.27) and (7.43), we obtain:

$$\int_0^T\int_\Omega |\chi(m)||\nabla\phi||\nabla c|\,dx\,dt \le \chi\,C^*\,C_{p'}\,H_2^{(b-s)}C\,H_3\|m\|^s_{L^p(\Omega_T)} . \tag{7.44}$$

Collecting all the above estimates (7.35), (7.38), (7.39) and (7.44), and (7.36), (7.37) and (7.40), and summing we have:

$$\int_0^T\int_\Omega (m+c)\,\theta\,dxdt \le \le C_1 + C_2\,\|m+c\|^\sigma_{L^p(\Omega_T)} + C_3\,\|m+c\|^s_{L^p(\Omega_T)} .$$

The above inequality holds for every $\theta \ge 0$ with $\|\theta\|_{L^{p'}(\Omega_T)} \le 1$, then, by the definition of the norm $L^p(\Omega_T)$ using duality we have that

$$\|m+c\|_{L^p(\Omega_T)} \le C_1 + C_2\,\|m+c\|^\sigma_{L^p(\Omega_T)} + C_3\,\|m+c\|^s_{L^p(\Omega_T)} ,$$

with σ and $s \in (0,1)$. Using Young's inequality, we obtain (7.28), and the constant H_p^* depends obviously on p, Ω, T, n, ϵ, τ, β, δ, $\|m_{in}\|_{W^{2-2/\bar{p},\bar{p}}(\Omega)}$, $\|c_{in}\|_{W^{2-2/\bar{p},\bar{p}}(\Omega)}$ and $\|d_{in}\|_{L^\infty(\Omega)}$, but not on λ. □

We are now ready to prove that the set Φ is bounded.

Lemma 7.11. *Under the hypotheses of Theorem 7.1, the set Φ is bounded in $C^{0,1}\times C^{0,1}$. In particular, if (m,c) are in Φ then*

$$\|m\|_{C^{0,1}} + \|c\|_{C^{0,1}} \le D_T , \tag{7.45}$$

where D_T is a constant which depends on Ω, T, n, ϵ, τ, β, δ and $\|m_{in}\|_{W^{2-2/\bar{p},\bar{p}}(\Omega)}$, $\|c_{in}\|_{W^{2-2/\bar{p},\bar{p}}(\Omega)}$, $\|d_{in}\|_{L^\infty(\Omega)}$, but not on λ.

Proof. As $p > n+2$, then $W_p^{1,2}(\Omega_T)$ is compactly embedded in $C^{0,1}$. Applying the maximal regularity results to the equation for c in (7.18a) we have that

$$\|c\|_{C^{0,1}} \le C\|c\|_{W_p^{1,2}(\Omega_T)} \le C_T\left(\delta\|d\|_{L^p(\Omega_T)} + \beta\|m\|_{L^p(\Omega_T)} + \|c_{in}\|_{W^{p,2-2/p}(\Omega)}\right) \le B_T , \tag{7.46}$$

where C_T depends on Ω, T, n, p and B_T depends on $\Omega, T, n, p, \epsilon, \tau, \beta, \delta$ and $\|m_{in}\|_{L^\infty(\Omega)}$, $\|c_{in}\|_{L^\infty(\Omega)}$ and $\|d_{in}\|_{L^\infty(\Omega)}$, but not on λ (see Lemma 7.10 and (7.15)).

Repeating for the m-equation in (7.18a) the same argument, we have:

$$\|m\|_{C^{0,1}} \le C\|m\|_{W_p^{1,2}(\Omega_T)}$$

$$\leq C_T \left(\|m(1-m)\, c - \chi(m)\Delta c\|_{L^p(\Omega_T)} + \|m_{in}\|_{W^{p,2-2/p}(\Omega)} \right) \leq B_T^* \,. \tag{7.47}$$

Consequently, (7.45) is proved using (7.46) and (7.47). □

7.1.4. Existence of the solution

We conclude this subsection by proving the existence of a global solution. This is stated by the following Proposition whose proof is a consequence of Lemmas 7.4, 7.5, 7.6, and 7.11:

Proposition 7.12. *Under the hypotheses of Theorem 7.1, for any $T > 0$, the system (7.1) with Neumann boundary conditions (7.2) and initial data (7.3) admits, in $[0,T]$, a strong non negative solution (m,c,d). Moreover there exists a constant C, which depends on Ω, T, n, ϵ, τ, β, δ and $\|m_{in}\|_{W^{2-2/\bar{p},\bar{p}}(\Omega)}$, $\|c_{in}\|_{W^{2-2/\bar{p},\bar{p}}(\Omega)}$, $\|d_{in}\|_{L^\infty(\Omega)}$, such that:*

$$\|m\|_{C^{0,1}} + \|c\|_{C^{0,1}} + \|d\|_{L^\infty(\Omega_T)} \leq C \,. \tag{7.48}$$

Proof. Using the Leray–Schauder fixed point theorem, we have that S admits a fixed point.

Then, for any $T > 0$, one can obtain in $[0,T]$ a solution of the original system (7.1).

The inequality (7.48) follows from (7.15) and (7.45).

Moreover, as all terms appearing in the system (7.1) are defined a.e. as $L^1(\Omega_T)$ functions, then the solution is strong. □

7.2. Uniqueness

In this subsection we shall prove that the solution of system (7.1) with boundary conditions (7.2) and initial conditions (7.3) is unique. Namely, we shall prove the following

Proposition 7.13. *Under the hypotheses of Theorem 7.1 and for each $T > 0$, the solution to system (7.1) with Neumann boundary conditions (7.2) and initial data (7.3) constructed in Proposition 7.12 is unique.*

Proof. Let (m_1, c_1, d_1) and (m_2, c_2, d_2) be two solutions of system (7.1), with boundary and initial conditions given in (7.2) and (7.3). Taking their differences, we have:

$$\frac{d}{dt}\int_\Omega |d_1 - d_2|^2 dx \leq$$
$$r(1 + H_0 + \|m_2\|_{L^\infty(\Omega_T)}) \left(\int_\Omega |m_1 - m_2|^2 dx + \int_\Omega |d_1 - d_2|^2 dx \right) , \tag{7.49a}$$

$$\frac{d}{dt}\int_\Omega |c_1 - c_2|^2 dx + \frac{2\epsilon}{\tau}\int_\Omega |\nabla(c_1 - c_2)|^2 dx \leq$$
$$\frac{\beta}{\tau}\int_\Omega |m_1 - m_2|^2 dx + \frac{\delta}{\tau}\int_\Omega |d_1 - d_2|^2 dx$$
$$+ \frac{\beta+\delta}{\tau}\int_\Omega |c_1 - c_2|^2 dx \,, \tag{7.49b}$$

$$\frac{d}{dt}\int_\Omega |m_1 - m_2|^2 dx + 2\int_\Omega |\nabla(m_1 - m_2)|^2 dx$$
$$+2\int_\Omega c_1 (m_1 + m_2)(m_1 - m_2)^2 dx =$$
$$\leq 2\|c_1\|_{L^\infty(\Omega_T)} \int_\Omega |m_1 - m_2|^2 dx$$
$$+\|m_2\|_{L^\infty(\Omega_T)}(1 + \|m_2\|_{L^\infty(\Omega_T)}) \left(\int_\Omega |c_1 - c_2|^2 dx + \int_\Omega |m_1 - m_2|^2 dx \right)$$
$$+ \int_\Omega \chi^2 |\nabla(c_1 - c_2)|^2 dx + \int_\Omega |\nabla(m_1 - m_2)|^2 dx$$
$$+\chi^2 \|\nabla c_1\|_{L^\infty(\Omega_T)} \int_\Omega |m_1 - m_2|^2 dx$$
$$+ \int_\Omega |\nabla(m_1 - m_2)|^2 dx \,. \tag{7.49c}$$

From (7.49c) we get:

$$\frac{d}{dt}\int_\Omega |m_1 - m_2|^2 dx \leq$$
$$\|m_2\|_{L^\infty(\Omega_T)}(1 + \|m_2\|_{L^\infty(\Omega_T)}) \int_\Omega |c_1 - c_2|^2 dx$$
$$+\chi^2 \int_\Omega |\nabla(c_1 - c_2)|^2 dx$$
$$+ \left(2\|c_1\|_{L^\infty(\Omega_T)} + \|m_2\|_{L^\infty(\Omega_T)}(1 + \|m_2\|_{L^\infty(\Omega_T)}) + \chi^2 \|\nabla c_1\|_{L^\infty(\Omega_T)} \right)$$
$$\times \int_\Omega |m_1 - m_2|^2 dx$$
$$\leq A \int_\Omega |c_1 - c_2|^2 dx + \chi^2 \int_\Omega |\nabla(c_1 - c_2)|^2 dx$$
$$+B \int_\Omega |m_1 - m_2|^2 dx \,. \tag{7.49d}$$

with $A = \|m_2\|_{L^\infty(\Omega_T)}(1 + \|m_2\|_{L^\infty(\Omega_T)})$ and $B = 2\|c_1\|_{L^\infty(\Omega_T)} + \|m_2\|_{L^\infty(\Omega_T)}(1 + \|m_2\|_{L^\infty(\Omega_T)}) + \chi^2 \|\nabla c_1\|_{L^\infty(\Omega_T)}$. Using the previous estimates (7.49a)–(7.49b)–(7.49d) and applying the Gronwall's lemma to:

$$\int_\Omega |m_1 - m_2|^2 \, dx + \frac{\tau\chi^2}{2\epsilon}\int_\Omega |c_1 - c_2|^2 \, dx + \int_\Omega |d_1 - d_2|^2 \, dx,$$

we obtain:

$$\int_\Omega |m_1 - m_2|^2 dx + \frac{\tau\chi^2}{2\epsilon}\int_\Omega |c_1 - c_2|^2 dx + \int_\Omega |d_1 - d_2|^2 dx \leq$$
$$\leq e^{\Xi t} \left(\int_\Omega |m_{1in} - m_{2in}|^2 dx + \frac{\tau\chi^2}{2\epsilon}\int_\Omega |c_{1in} - c_{2in}|^2 dx \right.$$
$$\left. + \int_\Omega |d_{1in} - d_{2in}|^2 dx \right) ,$$

where

$$\Xi = \max \left(r(1 + H_0 + \|m_2\|_{L^\infty(\Omega_T)}) + B + \frac{\beta\chi^2}{2\epsilon}; \frac{\beta+\delta}{\tau} + \frac{2A\epsilon}{\tau\chi^2}; \right.$$
$$\left. r(1 + H_0 + \|m_2\|_{L^\infty(\Omega_T)}) + \frac{\delta\chi^2}{2\epsilon} \right) ,$$

so that the uniqueness of the solution is proved. □

Propositions 7.12 and 7.13 give Theorem 7.1.

8. Conclusions

Despite the profound impact of MS on individuals and society, mathematical research focused on MS has been underwhelming to date. Nevertheless, mathematical modeling of MS has yielded numerous insights into its pathophysiology, progression, therapeutic strategies, and potential treatment strategies [26].

In this paper, we have studied a reaction–diffusion-chemotaxis model of MS that extends the system proposed in [33] by including the triggering effect of cytokines in the activation rate of macrophages. Since activated T-cells release cytokines in the early stages of plaque formation [21,40,41], the proposed system is an initial attempt to account for the involvement of the adaptive immune system while maintaining a mathematically simple description. Notably, the combined effect of innate and adaptive immune responses on the development of MS is recently described in [37], where the authors combine the ODE-based description of peripheral triggering by T-cells with the PDE-based description (derived from [33]) of the innate response in the brain parenchyma. In this work, we introduce the effects of T-cell-produced cytokines on macrophage activation while keeping the simplified description of [33] and retaining three interacting species. This choice facilitates a mathematical investigation of the instabilities responsible for lesion formation. We characterize the chemotaxis-driven Turing instability through a weakly nonlinear analysis near the homogeneous equilibrium and construct the corresponding stationary patterns. These asymptotic solutions of the model system are obtained for biologically

measured values of the system parameters and qualitatively reproduce the concentric demyelinating rings observed in Balò sclerosis and in type III MS. Through extensive numerical simulations on 2D domains, we investigate the onset and progression of the plaques The comparison with the results obtained in [33], where direct activation of macrophages with no involvement of cytokines was assumed, reveals a less aggressive pathology. This form of the disease displays lower levels of inflammation and evolves on significantly slower timescales. Moreover, we prove the existence of a unique global solution to the proposed system when the activation rate grows linearly with increasing cytokine levels. We believe this result, which does not immediately derive from the previously published well-posedness theorems on [33], is of independent interest.

This paper does not consider several issues that could be the subject of further investigation. One line of research worth exploring involves considering the dependence of the diffusion coefficient on cell density. It is well-documented that variations in cellular density at the lesion site can lead to differences in diffusivity [77]. While a recent study [55] describes this effect, its potential consequences on lesion development and progression have yet to be addressed.

Furthermore, the rigorous construction of axisymmetric stationary patterns on 2D domains is of significant interest [35].

The nonlinear stability of the proposed model using a suitable Lyapunov functional is also worth investigating [78,79].

A hyperbolic extension of the parabolic system introduced here would enable the exploration of inertial effects and the modeling of transient dynamics between the homogeneous steady state and the asymptotic stationary pattern [80].

Finally, examining the mechanisms leading to the emergence of localized plaques deserves attention. The pattern localization could occur under specific parameter regimes, where the homoclinic snaking scenario verifies, or as a consequence of the spatial heterogeneity of the cerebral tissue, [81]. Both of these scenarios will be the focus of subsequent work.

CRediT authorship contribution statement

F. Gargano: Writing – review & editing, Writing – original draft, Methodology, Investigation, Conceptualization. **M.C. Lombardo:** Writing – review & editing, Writing – original draft, Methodology, Investigation, Conceptualization. **R. Rizzo:** Writing – review & editing, Writing – original draft, Methodology, Investigation, Conceptualization. **M. Sammartino:** Writing – review & editing, Supervision, Investigation, Conceptualization. **V. Sciacca:** Writing – review & editing, Writing – original draft, Methodology, Investigation, Conceptualization.

Declaration of competing interest

The authors declare that they have no known competing financial interests or personal relationships that could have appeared to influence the work reported in this paper.

Data availability

No data was used for the research described in the article.

Acknowledgments

This work has been supported by the MUR-PRIN2017 grant: *Multiscale phenomena in continuum mechanics: singular limits, off-equilibrium and transitions* (project no.2017YBKNCE) and by the MUR-PRIN2022 grant: *Evolution problems involving interacting scales* (project no. 2022M9BKBC_00). The authors also gratefully acknowledge the financial support of GNFM-INdAM and the FFR2022-FFR2023 grant of the University of Palermo. RR acknowledges to have been co-funded by the European Union-ESF, PON Research and Innovation 2014–2020 - Ministerial Decree 1062/2021.

References

[1] C.A. Dendrou, L. Fugger, M.A. Friese, Immunopathology of multiple sclerosis, Nat. Rev. Immunol. 15 (9) (2015) 545–558.
[2] B. Hemmer, M. Kerschensteiner, T. Korn, Role of the innate and adaptive immune responses in the course of multiple sclerosis, Lancet Neurol. 14 (4) (2015) 406–419.
[3] K.E. Attfield, L.T. Jensen, M. Kaufmann, M.A. Friese, L. Fugger, The immunology of multiple sclerosis, Nat. Rev. Immunol. 22 (12) (2022) 734–750.
[4] J. Merrill, N. Scolding, Mechanisms of damage to myelin and oligodendrocytes and their relevance to disease, Neuropathol. Appl. Neurobiol. 25 (6) (1999) 435–458.
[5] X.-M. Zhang, H. Lund, S. Mia, R. Parsa, R.A. Harris, Adoptive transfer of cytokine-induced immunomodulatory adult microglia attenuates experimental autoimmune encephalomyelitis in DBA/1 mice, Glia 62 (5) (2014) 804–817.
[6] J. Yin, K. Valin, M. Dixon, J. Leavenworth, The role of microglia and macrophages in CNS homeostasis, autoimmunity, and cancer, J. Immunol. Res. 2017 (2017) 5150678.
[7] N. Abe, T. Nishihara, T. Yorozuya, J. Tanaka, Microglia and macrophages in the pathological central and peripheral nervous systems, Cells 9 (9) (2020).
[8] E. Kamma, W. Lasisi, C. Libner, H. Ng, J. Plemel, Central nervous system macrophages in progressive multiple sclerosis: Relationship to neurodegeneration and therapeutics, J. Neuroinflammation 19 (1) (2022).
[9] B.B. Guillemin GJ, Microglia, macrophages, perivascular macrophages, and pericytes: A review of function and identification, J. Leukoc. Biol. 75 (3) (2004) 388–397.
[10] M. Schwartz, Macrophages and microglia in central nervous system injury: Are they helpful or harmful? J. Cerebral Blood Flow Metabol. 23 (4) (2003) 385–394.
[11] Y. Li, N. Chu, A. Hu, B. Gran, A. Rostami, G.-X. Zhang, Increased IL-23p19 expression in multiple sclerosis lesions and its induction in microglia, Brain 130 (2) (2007) 490–501.
[12] N. Moise, A. Friedman, A mathematical model of the multiple sclerosis plaque, J. Theoret. Biol. 512 (2021) 110532.
[13] L. Peferoen, D. Vogel, K. Ummenthum, M. Breur, P. Heijnen, W. Gerritsen, R. Peferoen-Baert, P. Van Der Valk, C. Dijkstra, S. Amor, Activation status of human microglia is dependent on lesion formation stage and remyelination in multiple sclerosis, J. Neuropathol. Exp. Neurol. 74 (1) (2015) 48–63.
[14] J.-M. Zhang, J. An, Cytokines, inflammation, and pain, Int. Anesthesiol. Clin. 45 (2) (2007) 27–37.
[15] N. Ghasemi, S. Razavi, E. Nikzad, Multiple sclerosis: Pathogenesis, symptoms, diagnoses and cell-based therapy, Cell J. 19 (1) (2017) 1–10.
[16] C. Lucchinetti, W. Brück, J. Parisi, B. Scheithauer, M. Rodriguez, H. Lassmann, Heterogeneity of multiple sclerosis lesions: Implications for the pathogenesis of demyelination, Ann. Neurol. 47 (6) (2000) 707–717.
[17] P. Van Der Valk, C. De Groot, Staging of multiple sclerosis (MS) lesions: Pathology of the time frame of MS, Neuropathol. Appl. Neurobiol. 26 (1) (2000) 2–10.
[18] C. Lubetzki, B. Stankoff, Demyelination in multiple sclerosis, in: Handbook of clinical neurology, vol. 122, Elsevier, 2014, pp. 89–99.
[19] M. Sospedra, R. Martin, Immunology of multiple sclerosis, Sem. Neurol. 36 (2) (2016) 115–127.
[20] M. Barnett, J. Prineas, Relapsing and remitting multiple sclerosis: Pathology of the newly forming lesion, Ann. Neurol. 55 (4) (2004) 458–468.
[21] C. Marik, P. Felts, J. Bauer, H. Lassmann, K. Smith, Lesion genesis in a subset of patients with multiple sclerosis: A role for innate immunity? Brain 130 (11) (2007) 2800–2815.
[22] J. Baló, Encephalitis periaxialis concentrica, Arch. Neurol. Psychiatry 19 (2) (1928) 242–264.
[23] R. Kumar, G. Clermont, Y. Vodovotz, C. Chow, The dynamics of acute inflammation, J. Theoret. Biol. 230 (2) (2004) 145–155.
[24] K. Penner, B. Ermentrout, D. Swigon, Pattern formation in a model of acute inflammation, SIAM J. Appl. Dyn. Syst. 11 (2) (2012) 629–660.
[25] V. Giunta, M.C. Lombardo, M. Sammartino, Pattern formation and transition to chaos in a chemotaxis model of acute inflammation, SIAM J. Appl. Dyn. Syst. 20 (4) (2021) 1844–1881.
[26] G. Weatherley, R.P. Araujo, S.J. Dando, A.L. Jenner, Could mathematics be the key to unlocking the mysteries of multiple sclerosis? Bull. Math. Biol. 85 (8) (2023).
[27] W. Zhang, L.M. Wahl, P. Yu, Modeling and analysis of recurrent autoimmune disease, SIAM J. Appl. Math. 74 (6) (2014) 1998–2025.
[28] E. Kotelnikova, N. Kiani, E. Abad, E. Martinez-Lapiscina, M. Andorra, I. Zubizarreta, I. Pulido-Valdeolivas, I. Pertsovskaya, L. Alexopoulos, T. Olsson, R. Martin, F. Paul, J. Tegnér, J. Garcia-Ojalvo, P. Villoslada, Dynamics and heterogeneity of brain damage in multiple sclerosis, PLoS Comput. Biol. 13 (10) (2017).
[29] M. Elettreby, E. Ahmed, A simple mathematical model for relapsing-remitting multiple sclerosis (RRMS), Med. Hypotheses 135 (2020).
[30] R. Khonsari, V. Calvez, The origins of concentric demyelination: Self-organization in the human brain, PLoS One 2 (1) (2007) e150.

[31] V. Calvez, R. Khonsari, Mathematical description of concentric demyelination in the human brain: Self-organization models, from Liesegang rings to chemotaxis, Math. Comput. Modelling 47 (7–8) (2008) 726–742.

[32] R. Barresi, E. Bilotta, F. Gargano, M. Lombardo, P. Pantano, M. Sammartino, Wavefront invasion for a chemotaxis model of multiple sclerosis, Ric. Mat. 65 (2) (2016) 423–434.

[33] M. Lombardo, R. Barresi, E. Bilotta, F. Gargano, P. Pantano, M. Sammartino, Demyelination patterns in a mathematical model of multiple sclerosis, J. Math. Biol. 75 (2) (2017) 373–417.

[34] E. Bilotta, F. Gargano, V. Giunta, M.C. Lombardo, P. Pantano, M. Sammartino, Eckhaus and zigzag instability in a chemotaxis model of multiple sclerosis, AAPP Atti della Accademia Peloritana dei Pericolanti, Classe di Scienze Fisiche, Matematiche e Naturali 96 (2018) Article n. A9.

[35] E. Bilotta, F. Gargano, V. Giunta, M. Lombardo, P. Pantano, M. Sammartino, Axisymmetric solutions for a chemotaxis model of multiple sclerosis, Ric. Mat. 68 (1) (2019) 281–294.

[36] M. Bisi, M. Groppi, G. Martalò, C. Soresina, A chemotaxis reaction–diffusion model for multiple sclerosis with Allee effect, Ric. Mat. 73 (2024) 29–46.

[37] M.A.M. de Paula, B. de Melo Quintela, M. Lobosco, On the use of a coupled mathematical model for understanding the dynamics of multiple sclerosis, J. Comput. Appl. Math. 428 (2023).

[38] E.D. Ponomarev, L.P. Shriver, K. Maresz, J. Pedras-Vasconcelos, D. Verthelyi, B.N. Dittel, GM-CSF production by autoreactive T cells is required for the activation of microglial cells and the onset of experimental autoimmune encephalomyelitis, J. Immunol. 178 (1) (2007) 39–48.

[39] H. Lassmann, J. Van Horssen, The molecular basis of neurodegeneration in multiple sclerosis, FEBS Lett. 585 (23) (2011) 3715–3723.

[40] E.M. Frohman, M.K. Racke, C.S. Raine, Medical progress: Multiple sclerosis - The plaque and its pathogenesis, N. Engl. J. Med. 354 (9) (2006) 942–955.

[41] H. Lassmann, Multiple sclerosis pathology, Cold Spring Harbor Perspect. Med. 8 (3) (2018).

[42] D. Boche, V. Perry, J. Nicoll, Review: Activation patterns of microglia and their identification in the human brain, Neuropathol. Appl. Neurobiol. 39 (1) (2013) 3–18.

[43] E. Keller, L. Segel, Initiation of slime mold aggregation viewed as an instability, J. Theoret. Biol. 26 (3) (1970) 399–415.

[44] T. Hillen, K. Painter, Global existence for a parabolic chemotaxis model with prevention of overcrowding, Adv. Appl. Math. 26 (4) (2001) 280–301.

[45] Y. Dolak, C. Schmeiser, The keller-segel model with logistic sensitivity function and small diffusivity, SIAM J. Appl. Math. 66 (1) (2006) 286–308.

[46] D. Wrzosek, Global attractor for a chemotaxis model with prevention of overcrowding, Nonlinear Anal. TMA 59 (8) (2004) 1293–1310.

[47] N. Bellomo, A. Bellouquid, Y. Tao, M. Winkler, Toward a mathematical theory of Keller-Segel models of pattern formation in biological tissues, Math. Models Methods Appl. Sci. 25 (9) (2015) 1663–1763.

[48] T. Suzuki, Free Energy and Self-Interacting Particles, in: Progress in Nonlinear Differential Equations and Their Applications, vol. 62, Birkhäuser Boston, MA, 2005.

[49] M. Burger, M. Di Francesco, Y. Dolak-Struss, The Keller-Segel model for chemotaxis with prevention of overcrowding: Linear vs. Nonlinear diffusion, SIAM J. Math. Anal. 38 (4) (2006) 1288–1315.

[50] P. Zheng, C. Mu, X. Hu, Boundedness and blow-up for a chemotaxis system with generalized volume-filling effect and logistic source, Discrete Contin. Dyn. Syst. Ser. A 35 (5) (2015) 2299–2323.

[51] J. Zheng, Boundedness of solutions to a quasilinear parabolic-elliptic keller-segel system with logistic source, J. Differential Equations 259 (1) (2015) 120–140.

[52] X. Hu, S. Fu, S. Ai, Global asymptotic behavior of solutions for a parabolic-parabolic-ODE chemotaxis system modeling multiple sclerosis, J. Differential Equations 269 (9) (2020) 6875–6898.

[53] L. Desvillettes, V. Giunta, Existence and regularity for a chemotaxis model involved in the modeling of multiple sclerosis, Ric. Mat. 70 (1) (2021) 99–113.

[54] L. Desvillettes, V. Giunta, J. Morgan, B. Tang, Global well-posedness and nonlinear stability of a chemotaxis system modelling multiple sclerosis, Proc. R. Soc. Edinb. A 152 (4) (2022) 826–856.

[55] S. Fagioli, E. Radici, L. Romagnoli, On a chemotaxis-haptotaxis model with nonlinear diffusion modelling multiple sclerosis, 2023, Preprint.

[56] J.D. Murray, third ed., Mathematical Biology, vol. II, Springer, New York, 2007.

[57] M. Luca, A. Chavez-Ross, L. Edelstein-Keshet, A. Mogilner, Chemotactic signaling, microglia, and Alzheimer's disease senile plaques: Is there a connection? Bull. Math. Biol. 65 (4) (2003) 693–730.

[58] A. Nimmerjahn, F. Kirchhoff, F. Helmchen, Resting microglial cells are highly dynamic surveillants of brain parenchyma in vivo, Neuroforum 11 (3) (2005) 95–96.

[59] C. Lucchinetti, W. Brück, J. Parisi, B. Scheithauer, M. Rodriguez, H. Lassmann, A quantitative analysis of oligodendrocytes in multiple sclerosis lesions. a study of 113 cases, Brain 122 (12) (1999) 2279–2295.

[60] P. Moghe, R. Nelson, R. Tranquillo, Cytokine-stimulated chemotaxis of human neutrophils in a 3-D conjoined fibrin gel assay, J. Immunol. Methods 180 (2) (1995) 193–211.

[61] G. Goodhill, Diffusion in axon guidance, Eur. J. Neurosci. 9 (7) (1997) 1414–1421.

[62] S. Lee, W. Liu, D. Dickson, C. Brosnan, J. Berman, Cytokine production by human fetal microglia and astrocytes: Differential induction by lipopolysaccharide and IL-1β, J. Immunol. 150 (7) (1993) 2659–2667.

[63] S. Nagaraja, A. Wallqvist, J. Reifman, A. Mitrophanov, Computational approach to characterize causative factors and molecular indicators of chronic wound inflammation, J. Immunol. 192 (4) (2014) 1824–1834.

[64] G. Gambino, M. Lombardo, M. Sammartino, Pattern formation driven by cross-diffusion in a 2D domain, Nonlinear Anal. RWA 14 (3) (2013) 1755–1779.

[65] G. Gambino, V. Giunta, M.C. Lombardo, G. Rubino, Cross-diffusion effects on stationary pattern formation in the Fitzhugh-Nagumo model, Discrete Contin. Dyn. Syst. Ser. B 27 (12) (2022) 7783–7816.

[66] G. Gambino, M.C. Lombardo, R. Rizzo, M. Sammartino, Excitable FitzHugh-Nagumo model with cross-diffusion: Long-range activation instabilities, Ric. Mat. 73 (1) (2024) 115–135.

[67] G. Gambino, M.C. Lombardo, R. Rizzo, M. Sammartino, Excitable FitzHugh-Nagumo model with cross-diffusion: close and far-from-equilibrium coherent structures, Ric. Mat. 73 (1) (2023) 137–156.

[68] G. Gambino, M. Lombardo, M. Sammartino, Turing instability and traveling fronts for a nonlinear reaction-diffusion system with cross-diffusion, Math. Comput. Simulation 82 (6) (2012) 1112–1132.

[69] C. De Groot, E. Bergers, W. Kamphorst, R. Ravid, C. Polman, F. Barkhof, P. Van Der Valk, Post-mortem MRI-guided sampling of multiple sclerosis brain lesions: Increased yield of active demyelinating and (p)reactive lesions, Brain 124 (8) (2001) 1635–1645.

[70] J. van Horssen, S. Singh, S. van der Pol, M. Kipp, J. Lim, L. Peferoen, W. Gerritsen, E.-J. Kooi, M. Witte, J. Geurts, H. de Vries, R. Peferoen-Baert, P. van den Elsen, P. van der Valk, S. Amor, Clusters of activated microglia in normal-appearing white matter show signs of innate immune activation, J. Neuroinflammation 9 (2012).

[71] C. Stadelmann, S. Ludwin, T. Tabira, A. Guseo, C. Lucchinetti, L. Leel-Ossy, A. Ordinario, W. Brück, H. Lassmann, Tissue preconditioning may explain concentric lesions in Baló's type of multiple sclerosis, Brain 128 (5) (2005) 979–987, http://dx.doi.org/10.1093/brain/awh457, Epub 2005 Mar 17.

[72] A.R. Cañellas, A.R. Gols, J.R. Izquierdo, M.T. Subirana, X.M. Gairin, Idiopathic inflammatory-demyelinating diseases of the central nervous system, Neuroradiology 49 (5) (2007) 393–409, http://dx.doi.org/10.1007/s00234-007-0216-2.

[73] D. Gilbarg, N. Trudinger, Elliptic Partial Differential Equations of Second Order, Berlin Heidelberg, in: Classics in Mathematics, Springer, 2001.

[74] O. Ladyzenskaija, V.A. Solonnikov, N. Ural'ceva, Linear and Quasi-Linear Equations of Parabolic Type, in: Translations of Mathematical Monographs, vol. 23, American Mathematical Society, 1988, p. 648.

[75] J. Simon, Compact sets in the space $L^p(0,T;B)$, Ann. Mat. Pura Appl. 146 (1) (1986) 65–96.

[76] A. Mayda, A. Bertozzi, Vorticity Abd Incompressible Flow, Cambridge University Press, 2002.

[77] S. Serres, D.C. Anthony, Y. Jiang, S.J. Campbell, K.A. Broom, A. Khrapitchev, N.R. Sibson, Comparison of MRI signatures in pattern I and II multiple sclerosis models, NMR Biomed. 22 (10) (2009) 1014–1024.

[78] G. Arnone, F. Capone, Density inversion phenomenon in porous penetrative convection, Int. J. Non-Linear Mech. 147 (2022) 104198.

[79] F. Capone, M. Carfora, R. De Luca, I. Torcicollo, Nonlinear stability and numerical simulations for a reaction-diffusion system modelling Allee effect on predators, Int. J. Nonlinear Sci. Numer. Simul. 23 (5) (2022) 751–760.

[80] G. Grifó, G. Consolo, C. Curró, G. Valenti, Rhombic and hexagonal pattern formation in 2D hyperbolic reaction–transport systems in the context of dryland ecology, Physica D 449 (2023).

[81] E. Gaffney, A. Krause, P. Maini, C. Wang, Spatial heterogeneity localizes turing patterns in reaction-cross-diffusion systems, Discrete Contin. Dyn. Syst. Ser. B 28 (12) (2023) 6092–6125.